Cross-shore Velocity Moments in the Nearshore: Validating SWASH

Xiaomin Liao

Master of Science Thesis

TU Delft Delft University of Technology

Cross-shore Velocity Moments in the Nearshore: Validating SWASH

Master of Science Thesis

For the degree of Master of Science in Coastal Engineering at Delft University of Technology

Xiaomin Liao

February 20, 2015

Faculty of Civil Engineering and Geosciences (CEG) · Delft University of Technology

Delft University of Technology
Department of
Civil Engineering and Geosciences (CEG)

Graduation committee

Prof. dr. ir. M.J.F. Stive	Delft University of Technology
Dr. ir. M. Zijlema	Delft University of Technology
MSc. S. Meirelles	Delft University of Technology
Ir. M. Henriquez	Delft University of Technology

Abstract

The cross-shore sediment transport is of great importance in the coastal water since it may lead to significant change of coastal profile. Many researches(e.g. Bailard [4]) have proved that the sediment transport is proportional to velocity moments. In this study, the velocity moments under wave action in the perpendicular direction to the coastline are studied by means of a non-hydrostatic model SWASH and a decomposition technique.

The purpose of this project is to perform the velocity moments which contribute to the cross-shore sediment transport with a numerical analysis and the most significant components can be found through the comparisons. These contributed flows to the velocity moments, namely asymmetric oscillatory flow, wave grouping-induced flow and undertow, are the major objects to be studied.

A set of measurements of wave flume experiment are adopted to evaluate the feasibility of the method developed in this study. Firstly, a series of sensitivity analysis of wave decay and mean velocity are presented to investigate the influence of varied settings in SWASH, including the vertical resolution, boundary imposition, bottom friction, discretization schemes for advection terms and water depth in velocity points. The results indicate that predictions of SWASH with proper settings are in good agreement with measurements in terms of wave decay and vertical velocity. Furthermore, a detailed analysis is subsequently conducted with regard to surface elevation, wave decay and undertow. Most of the SWASH predictions are in relatively good agreement with the measurements, but some deviations occurred after wave breaking. This is probably associated to the absence of the production of turbulent energy due to surface roller.

A signal decomposition technique is applied to separate the signals with different frequencies. Through the decomposition process, the long and short wave flows are separated by means of filtering out the other part. The SWASH predicted central odd moments of long wave flows is relatively underestimated while the long wave flow variances and the central odd moments of asymmetric flows agree well to the observations. This may correspond to the loss of signal information after decomposition. By summing up the contributions of undertow, wave grouping-induced long wave flow and asymmetric oscillatory flow, the total odd flow moment is easily acquired.

Generally, the offshore-directed undertow is the dominant component, the shoreward asymmetric flow is of secondary importance and the contribution of long wave flow is relatively small. As a consequence, the resulted total flow carries the sediment transporting seaward. In overall, SWASH is capable of simulating the wave decay and vertical flow structure correctly. However, some deviations near the breaking point implies that, implementation of breaking-induced turbulence in SWASH is of great importance.

Acknowledgements

This Master thesis marks the completion of the Master of Science program in Hydraulic at the Faculty of Civil Engineering and Geosciences, Delft University of Technology.

First and foremost, I would like to show my deepest gratitude to the members of my graduation committee. I would like to thank Prof.dr.ir. M.J.F. Stive for the motivation of the thesis topic as well as the support for finishing the project successfully. Many thanks to Marcel Zijlema for proving knowledge and advise to setup the model. I would also like to thank Martijn Henriquez and Dirk Rijnsdorp for the support during the master project.

A special thank is given to my daily supervisor Saulo Meirelles, for his responsible guidance through the whole project.

Last but not least, I would like to acknowledge my family and friends. I did have a tough time during this year but thanks to their support I conquered all the difficulties.

Delft, University of Technology — Xiaomin Liao
February 20, 2015

Table of Contents

List of Figures

List of Tables

Chapter 1

Introduction

The cross-shore velocity moments contributing to the sediment transport in the coastal waters are studied in this Master thesis, with the aim of providing a routine to investigate onshore-offshore sediment transport in the future study. This chapter firstly presents the background information. Relating to the currently known knowledge, the research question is introduced, which is followed by the objectives and research method.

1-1 Background

In order to design infrastructure in the coastal area or protect coastline, it is necessary to understand the coastal morphology thoroughly. The morphological changes in coastal region are the responses to the interactions between the fluid motions and sediments. Thus, the sediment transport is one of the most critical determinants of the coastal morphological evolution.

Firstly, it is vital to have an insight into the coastal profile. The coastal profile is defined as the shoreface extension from the shelf to the beach and the dune face. It can be divided into the lower shoreface, the upper shoreface and the back shore in the direction perpendicular to the coastline, given in Figure 1-1.

The lower shoreface is the region from the shelf edge to the outer surf zone with a slow response to the wave action; the upper shoreface is composed of the surf zone and the beach, this area adapts almost instantaneously to the change of profile; the backshore consists of some dunes and cliffs, it also present a relatively fast response to the wave action. Moreover, the backshore region acts as a barrier between the waves and inland, especially during the storm surge. Hence the dunes or the cliffs should be high enough to prevent overwash and even inundation to protect the coast and the hinterland [12]. Consequently, the bottom profile in the nearshore should be preserved in order to maintain the coastline and the infrastructure near backshore.

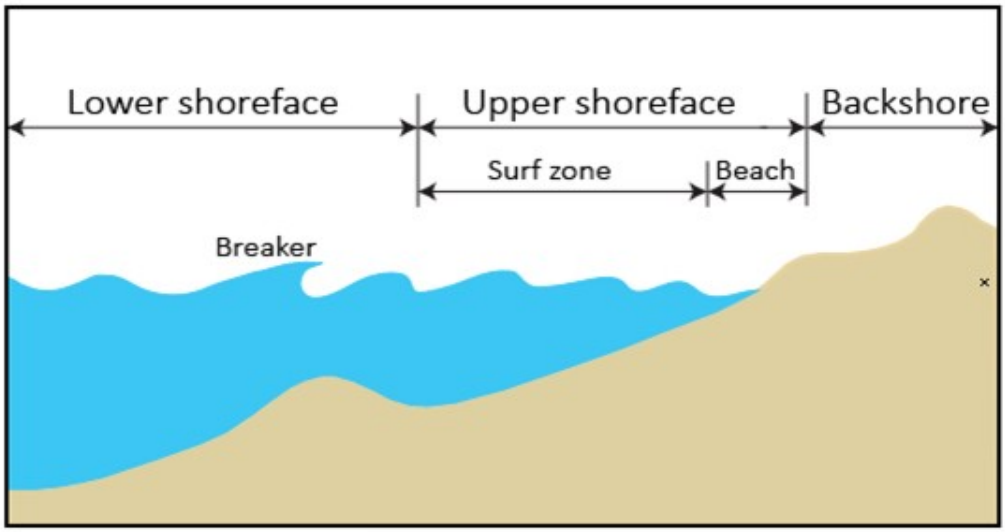

Figure 1-1: Different regions of coastal profile: lower shoreface, upper shoreface and backshore

The cross-shore sediment transport is one of the most critical determinants of the coastal profile evolution. Wright [27] has stressed that the coastal morphological processes are the responses to the fluid motions of the bottom boundary layer processes. Based on the law of momentum conservation, the moving fluid transmits the momentum to the sediments through the bottom boundary layer by means of friction forces. The sediments respond to the momentum transfer and start to move, resulting in sediment transport. The relevant gradients of transport in time and space lead to sediment erosion, transport and deposition, arousing the evolution of coastal morphology. It is thus of great importance to pay attention on the study regarding the dynamics of onshore-offshore sediment transport.

Various models have been developed to investigate the cross-shore sediment transport. A considerable number of these models are based on the energetic approach first raised by Bagnold [2][3]. Further, Bowen [9] rewrote the Bagnold's formulations for the immersed weight bed load and suspended load transport rates in the cross-shore direction. At the same stage, Bailard [4][6] summarized the Bagnold's model to a total load sediment transport model for time-varying flow over an arbitrarily plane slope. Moreover, the ability of Bailard's model to predict cross-shore sediment transport was evaluated [5], the result suggested that this model may be useful in studying onshore-offshore sediment movements.

In addition, Roelvink and Stive [21] simplified the formulations of Bailard by assuming that the velocity aligned with the local bed slope. In this case a simplified cross-shore transport model for the upper shore-face was developed. These simple formulations indicate that the sediment load transports are proportional to some power of the time varying flow velocity U near bed, given by:

$$\begin{aligned} &< S_b > \propto < U|U|^2 >, \quad \text{for bed load transport} \\ &< S_s > \propto < U|U|^3 >, \quad \text{for suspended load transport} \end{aligned}$$

The sediment transport is mainly a quasi-steady response to the time-varying flow represented by the odd velocity moments. In this study, we focus on the velocity moments which contribute to the bed load transport. Furthermore, Roelvink and Stive [21] indicated that the cross-shore flows induced in the nearshore may play a dominating role in the research of sediment transport and hence bar formation. These flows, namely the breaking-induced undertow, wave grouping-induced long wave flow and wave-induced asymmetric oscillatory flow, make different contributions to the sediment movements. As a result, the relevant contributions to the odd moments $< U|U|^2 >$ will be discussed separately in this Master thesis.

To accurately predict the cross-shore velocity moments, a model is required to calculate relevant flows. This work applies the non-hydrostatic wave-flow model SWASH since it is phase resolving and is capable of simulating a large number of phenomena in the nearshore correctly. In this case, the relevant nearshore processes may be computed in a potentially accurate manner.

In the past years, SWASH (Simulating WAves till SHore) has been developed at Delft University of Technology, providing efficient and robust computation for the transformation of shallow water flows in the coastal area up to the shore [29]. SWASH applies the nonlinear shallow water equations to provide a basic principle for simulating non-hydrostatic, free surface and rotational flows. The governing equations including the non-hydrostatic pressure are based on the Reynolds-averaged Navier-Stokes equations and mass balance equation. In this way, this numerical tool can be used to account for numerous nearshore processes, for instance, the wave transformation, propagation, breaking and vertical turbulent mixing, etc.

As indicated before, we are interested in the breaking-induced undertow, wave grouping-induced long wave flow and wave-induced asymmetric oscillatory flow. Some former studies have validated that SWASH is capable of simulating wave asymmetry and long wave accurately. The simulations of wave asymmetry and skewness by SWASH have a good agreement with measurements for mid-energetic conditions according to Brinkkemper[10]. In addition, Rijnsdorp et.al[20] have verified the capability of SWASH in simulating the cross-shore transformation of bound and free infra-gravity waves induced by the bi-chromatic waves. For a plane sloping bottom, SWASH correctly predicts the nearshore transformation of bound long waves but overestimates the magnitude of the outgoing free long waves. Nonetheless, SWASH makes overall good prediction for the wave grouping-induced long wave flow. Consequently, we do not go further into the prediction of wave skewness and long waves in this study, more attention is given to the simulation of undertow.

Finally, in order to have a general understanding of how SWASH resolves those onshore-offshore flows, this study reproduces the experiment conducted by Rovelvink and Stive [21].

1-2 Research Objectives

The aim of this research is providing a routine to calculate nearshore velocity moments in the cross-shore direction in a numerical way. Besides the numerical tool SWASH, a decomposition technique is necessary to filter low and high frequency components. Note that the further analysis of sediment transport will not be covered in this research.

In order to achieve the goal, the main objective is divided into sub objectives, which form the procedures in the project:

- Study the models of cross-shore sediment transport and analyse how do the velocity moments influence the sediment movements based on literature.
- Develop a efficient and reliable solving routine to compute the cross-shore flows and hence the relevant velocity moments.
- Validate the results of SWASH and the routine mentioned above by the application on a wave flume case.

1-3 Research Method

The study starts with a simple 1D model with the random waves propagating over a plane slope by SWASH. Based on the model result, the second step is creating the synthetic time series to decompose the signals in different components of velocity. In this way, the velocities of undertow, long wave flows and asymmetric flows can be obtained. Furthermore, the relevant cross-shore velocity moments can be calculated. In addition, this approach is applied to reproduce the wave flume experiments executed by Roelvink and Stive [21].

1-4 Outline

The purpose of this master thesis study is to investigate how the cross-shore flows contribute to the odd velocity moment $< U|U|^2 >$ by means of SWASH and decomposition technique. In Chapter 2, the knowledge required for accomplishing this study is interpreted. Various models of onshore-offshore sediment transport are studied and discussed to determine the optimal model which is further applied subsequently. Moreover, the methodology is described with regard to the numerical tool SWASH and the decomposition technique. Chapter 4 applies the method introduced in Chapter 3 to reproduce a wave flume experiment conducted by Roelvink and Stive [21]. The SWASH model is setup and the sensitivity study is carried out to determine the optimal settings. Furthermore, Chapter 5 presents the final result of the experiment, the contributions to the odd velocity moment in the onshore-offshore direction are compared and discussed to discover the most significant components. Lastly, the results are concluded and some recommendations are described in Chapter 6.

Chapter 2

Cross-shore Sediment Transport

This project aims to study on the cross-shore velocity moments related to sediment transport. Primarily, the knowledge of the processes concerning the cross-shore transport in the coastal area is essential to understand how the flows and velocity moments relate to the sediment transport. In this chapter, general aspects with regard to the cross-shore sediment transport are described.

Various models exist to study the cross-shore sediment movements. In section 2-1, 4 models of onshore-offshore sediment transport are illustrated to understand the relevant mechanism. The extensive analysis of the optimal model for this case is given in section 2-2, by decomposing the odd velocity moment which is proportional to the sediment transport. In this way, the odd velocity moment is decomposed into three components, namely the velocity moments related to undertow, long wave flow and asymmetric flow, respectively. Furthermore, the effect of each wave-induced cross-shore flow is discussed in section 2-3. Finally, section 2-4 shows result of the total flow moments.

2-1 Sediment Transport Models

In general, the theoretical models for sediment transport in the perpendicular direction to the coastline were developed from two distinct approaches: an energetic approach and a traction approach. The examples used in this section are based on the former approach developed by bagnold [2][3]. In this section, the models developed by Bagnold [2][3], Bowen [9], Bailard [4] and Roelvink and Stive [21] are indicated to gain insight into the cross-shore sediment transport and hence the relevant velocity moment.

2-1-1 Bagnold

Bagnold [2][3] was the first one who develop the energetic approach for the study of sediment transport. Bagnold assumed that a sufficient amount of energy is provided to keep the bed

load moving and the suspended load floating, the energy is depleted in transporting either the bed load or the suspended load by the stream. According to this assumption, the equation of sediment transport is hence proportional to the rate of energy dissipation of the stream flow.

Bagnold derives the following sediment transport formulations for bed load and suspended load for stream flow:

$$I_b = \frac{\varepsilon_b \omega}{tan\varphi_r - tan\alpha} \tag{2-1}$$

$$I_s = \frac{\varepsilon_s \omega}{w_s/U_s - tan\alpha} \tag{2-2}$$

in which,

I_b	immersed weight bed load transport rate
ε_b	bed load efficiency
I_s	immersed weight suspended load transport rate
ε_s	suspended load efficiency
ω	rate of energy dissipation of the stream
U_s	mean velocity of the stream
w_s	fall velocity of the sediment
φ_r	internal angle of friction of sediment
$tan\alpha$	slope of the stream bed

Bagnold's stream-based sediment transport model [3] is a relatively comprehensive approach to sedimentology. The information of flow is considered in the energy dissipation rate $\omega = \rho c_f U^2|U|$, where U is the time-dependent velocity. However, this model is for the steady uni-directional flow along the downward sloping bottom [2]. In the past decades, a number of models were developed for the onshore-offshore situation, based on the Bagnold's model, in order to make relatively accurate predictions of the cross-shore transport. A relatively complete onshore-offshore transport model was developed by Bowen [9], arising from Bagnold's model.

2-1-2 Bowen

Bowen [9] modified the equations for the situation of a cross-shore transport with normally incident waves according to the energetic-based model of Bagnold. Subsequently the expressions for the immersed weight bed load and suspended load transport rates are given by:

$$I_b = \frac{\varepsilon_b C_D \rho U^3}{tan\varphi_r - U tan\alpha/|U|} \tag{2-3}$$

$$I_s = \frac{\varepsilon_s C_D \rho U^3 |U|}{w_s - U tan\alpha} \tag{2-4}$$

in which,

U	time-dependent velocity
I_b	immersed weight bed load transport rate
ε_b	bed load efficiency
I_s	immersed weight suspended load transport rate
ε_s	suspended load efficiency
C_D	drag coefficient
ρ	water density
w_s	fall velocity of the sediment
φ_r	internal angle of friction of sediment
$tan\alpha$	slope of the stream bed

In order to develop a complete model with relatively adequate description of physical processes regarding sediment transport, there are additional conditions to limit the bed slope[1]:

$tan\alpha \rightarrow tan\varphi_r$	giving avalanching or slumping
$tan\alpha \rightarrow w_s/U$	giving the auto-suspension

Furthermore, the Taylor series is applied to expand the velocity moments in the Eq. (2-3) and Eq. (2-4). The author decomposed the velocity U into an orbital velocity U_0 and a perturbation U_1, where

$$U = U_0 + U_1 \tag{2-5}$$

By assuming the orbital velocity is the dominant motion, in other words, U_0 is much larger than $U_1 (U_0 \gg U_1)$, the Taylor expansion of the moment is given by:

$$U^n|U| = U_0^n|U_0| + (n+1)U_1U_0^{n-1}|U_0| + \frac{n(n+1)}{2}U_1^2U_0^{n-2}|U_0| + ... \tag{2-6}$$

There are numerous forms for perturbation U_1 , namely,

(1) A constant and steady current:

$$U_1 = u_1 \tag{2-7}$$

(2) Velocity field associated with a higher harmonic of the incoming wave:

$$U_1 = u_m cos(m\omega t + \theta_m), with\ \ m = 2, 3, 4... \tag{2-8}$$

(3) A perturbation due to a wave with frequency ω_t unrelated to ω:

$$U_1 = u_t cos(\omega_t t) \tag{2-9}$$

By this way, Bowen expanded the sediment transport formulations using the Taylor series mentioned above and took time-average of the expressions. Then the Bowen's transport formulations were obtained as the net transport over some periods. The model developed by Bowen provides a routine to decompose the flow signal and calculate the velocity moment. Based on this approach, Roelvink and Stive [21] derived another model by using Taylor expansion and some assumptions, which will be discussed later. In addition, this model does not consider the initiation of transport condition and both the bed load and suspended sediment movement adjust instantaneously to the changes of the flows.

2-1-3 Bailard

In the same period, Bailard [4][5] demonstrated a total load sediment transport model for time-varying flow over an arbitrarily plane slope. The author used the Bagnold's total sediment transport model [2][3] as working hypothesis to derive the model, the total load sediment transport equation is given as following:

$$\begin{aligned} < I_t(t) >= \rho c_f \frac{\varepsilon_b}{tan\varphi_r}[< U(t)|U(t)|^2 > - \frac{tan\alpha}{tan\varphi_r} < |U(t)|^3 >] \\ -\rho c_f \frac{\varepsilon_s}{w_s}[< U(t)|U(t)|^3 > - \frac{\varepsilon_s tan\alpha}{w_s} < |U(t)|^5 >] \end{aligned} \tag{2-10}$$

in which,

U	time-dependent velocity
I_t	immersed weight total load transport rate
ε_b	bed load efficiency
ε_s	suspended load efficiency
c_f	friction coefficient
ρ	water density
w_s	fall velocity of the sediment
φ_r	internal angle of friction of sediment
$tan\alpha$	slope of the stream bed
$\frac{\partial z_b}{\partial x}$	local bed slope

As can be seen in Eq. (2-10) that, the bed load and the suspended load are both composed of a primary component induced by velocity(directed parallel to the instantaneous velocity vector) and a secondary component related to gravity(directed down-slope). For the purpose of simplifying Eq. (2-10), Roelvink and Stive[21] rewrote the formulation in general terms, demonstrated in the following subsection.

2-1-4 Roelvink and Stive

Roelvink and Stive[21] have developed a model for the cross-shore sediment transport on the upper shoreface. The model indicated that the induced cross-shore flows, namely undertow, wave grouping-induced long wave flow, asymmetric oscillatory flow and turbulent flow, play vital roles in the study of onshore-offshore sediment transport.

The laboratory flume experiments were performed with random, grouped waves generated by a piston-type wave board with a rotation adjustment on a water depth of approximately 0.60m. Three experiments were conducted with the generated waves transmitting to two beach configurations respectively: one was carried out on a initially plane beach with a slope 1:40 and the other two were executed on a beach with a single bar with a same slope. Three tests were performed with different wave conditions as well, the experimental details and results will be discussed in Chapter 4.

Generally, the formulation for the sediment transport should be proportional to some power of the time-varying flow velocity near bed. An approximate example for the bed load transport is $< S_b > \propto < U|U|^2 >$ in which the angle brackets indicated time-averaging over a characteristic time period. The simple expression of sediment transport was derived from the formulation of Bailard [4] [5] and simplified by Roelvink and Stive[21], given as follows:

$$S(t) = Const_1 U(t)|U(t)|^n + Const_2|U(t)|^m \frac{\partial z_b}{\partial x} \tag{2-11}$$

where, $U(t)$ is the time-varying near-bottom cross-shore flow velocity, $\frac{\partial z_b}{\partial x}$ is the local bed slope. The power m and n determines the distinct modes of sediment transport, with n=2, m=3 for the bed load transport and n=3, m=5 for the suspended load transport, respectively.

This sediment transport formulation shows that the transport is composed of two parts: a quasi-steady response to the time-varying flow represented by the odd moments $< U(t)|U(t)|^2 >$ or $< U(t)|U(t)|^3 >$ and a down-slope directed transport induced by gravity force expressed by the even moments $< |U(t)|^3 >$ or $< |U(t)|^5 >$. Since the even moments are generally one order magnitude smaller than the odd moments, the following simplified statements could be applied:

$$\begin{aligned} &< S_b > \propto < U|U|^2 >, \quad \text{for bed load transport} \\ &< S_s > \propto < U|U|^3 >, \quad \text{for suspended load transport} \end{aligned}$$

The model of Roelvink and Stive provides a simple and efficient approach to solve cross-shore sediment transport problem. With this model, the relationship between the odd velocity moment and sediment transport is clear and hence this model is applied as the basis of this Master project. Note that we only focus on the odd velocity moment related to the bed load transport in this study.

2-2 Decomposition of the Velocity moments

As mentioned in the section 2-1-4 that, the sediment transport is mainly a quasi-steady response to the time-varying flow represented by the odd velocity moments. In order to figure out the relative contributions to the odd moments, a decomposition of the near-bottom flow velocity is done as follows:

$$U = \bar{U} + U_L + U_S \tag{2-12}$$

in which, $\bar{U}$ is the time-mean flow component, U_L represents the short wave averaged oscillatory component varying on the time scale of the wave groups and U_S reflects the short wave component on the time scale of the individual waves.

Then the Taylor series is applied to expand the odd velocity moment based on the research of Bowen [9]. By assuming $\bar{U} \ll U_L \ll U_S$, Roelvink and Stive [21] evaluated the contributions to the odd moment proportional to the bed load transport as seen below:

$$< U|U|^2 >= 3 < \bar{U}|U_S|^2 > + < U_S|U_S|^2 > +3 < U_L|U_S|^2 > \tag{2-13}$$

in which, the term $|U_S|^2$ indicates the sediment stirring induced by short waves. The first term in the RHS of the Eq. (2-13) $< \bar{U}|U_S|^2 >$ represents the contribution to the odd moment of the mean flow velocity. The relevant mean current in this case is represented by the offshore directed undertow induced by the wave breaking. The following term $< U_S|U_S|^2 >$ is the central, odd flow moment due to the wave asymmetry. The second term is zero when there is no short wave skewness and a positively skewed wave results in an onshore directed transport. The last term $< U_L|U_S|^2 >$ is related to the correlation between the long wave forced by the wave group and short wave velocity variance. Outside the surf zone, the trough of the group-forced bound long wave is found under the highest waves, stirring up more amount of sediment and transporting seaward. However, after the wave breaking point, the structure of bound long wave disappears. In the following section, general aspects of the relevant cross-shore flows are demonstrated.

2-3 Effects of wave-induced cross-shore flows

The most important contributions to the odd velocity moment which is proportional to the bed load transport have been discussed above. This section mainly focuses on the effects of relevant cross-shore flows, namely, the undertow, the wave asymmetry-induced oscillatory flow and the wave grouping-induced long-wave flow.

2-3-1 Undertow

As mentioned above in the Eq. (2-13), the first term $< \bar{U}|U_S|^2 >$ is related to the mean flow component. The contribution of mean flow is primarily due to the undertow. The undertow is defined as the offshore directed return flow compensating for the onshore mass flux above the trough level under the condition of wave breaking.

Roelvink and Stive [21] applied the Wave Energy Decay model to predict the wave height and water level set-up which are the basic elements to calculate the wave-induced flow motions. Hence a brief introduction of this model is present beforehand. The wave energy decay model was derived by Battjes and Janssen [7] in horizontal one-dimension with the calibrated parameters obtained by Battjes and Stive [8].

In order to calculate the undertow, the root-mean-square wave height, the mean water level set-up and the energy dissipation are predicted by the energy decay model. The predictions of the first two quantities have been proved to be satisfactory by the wave decay model. In addition, the dissipation of turbulent kinetic energy D may be derived with the aid of a one-equation model for the turbulent energy given by Launder and Spalding[16]. With these quantities, the undertow may be computed.

According to the undertow model described by Stive and De Vriend [24], the wave breaking induced shear stress $\tau(t)$ at trough level is proportional to the ratio of wave energy dissipation D to the wave phase speed c:

$$\tau(t) \propto \frac{D}{c} \tag{2-14}$$

This shear stress is the most important factor to drive the undertow. Based on the wave energy decay model, the term D is the dissipation source term of the turbulent kinetic energy, which generally lags behind the production term of turbulent energy P. Roelvink and Stive [21] have verified that the correction, using the term D instead of P, to the undertow model improves the prediction of undertow distribution.

Additionally, for the non-breaking waves, the mean flow could be the wave-induced Longuet-Higgins[17] streaming which is directed in the wave propagating direction, resulting in the shoreward directed sediment transport.

2-3-2 Wave asymmetry-induced flow

The term $< U_S|U_S|^2 >$ is associated with the short wave asymmetry and skewness in the surf zone. It is zero when there is no short wave skewness and a positively skewed wave results

in an onshore directed transport. It could be explained by the following reason: the velocity is larger under the wave crest leads to more sediment load stirred up by short waves and transported onshore. Consequently, the wave asymmetric oscillatory flow contributes to a shoreward directed net sediment transport.

2-3-3 Wave grouping-induced long-wave flow

The last term of the equation Eq. (2-13) $< U_L|U_S|^2 >$ indicates the contribution to the velocity moment of the correlation between the long wave forced by the wave group and short wave velocity variance. Outside the surf zone, the wave crest(onshore directed movement) of grouping-induced bound long wave coincides with the low waves while the trough(offshore directed movement) associates with the high waves. As a result, the negative correlation results in seaward directed transport before wave breaking. After the breaking bound long wave is realised and propagates as free long wave, hence the sediment transport in the region near beach is onshore directed.

2-4 Total flow moments

Based on the analysis of the undertow, the wave asymmetry-induced flow and the long-wave flow, the total flow moments could be obtained by adding these cross-shore flow velocity moments based on Eq. (2-13).

Roelvink and Stive[21] conducted the experiment with constant incident wave conditions of normal steepness for 12 hours on the beach of initially plane slope 1:40. The measurement of third and forth odd flow moments are showed in the Figure 2-1.

The curves in Figure 2-1 indicate the calculations of undertow, wave asymmetry-induced flow and wave grouping-induced long-wave flow based on model of Roelvink and Stive [21], respectively. The contribution of undertow is offshore directed while the asymmetric flow results in shoreward transport in the entire region of interest. The wave grouping-induced long wave contribution is seaward directed outside the surf zone and is onshore directed after breaking.

In this study, the results of the figure in the first panel are applied to make comparisons with the calculations conducted in this project.

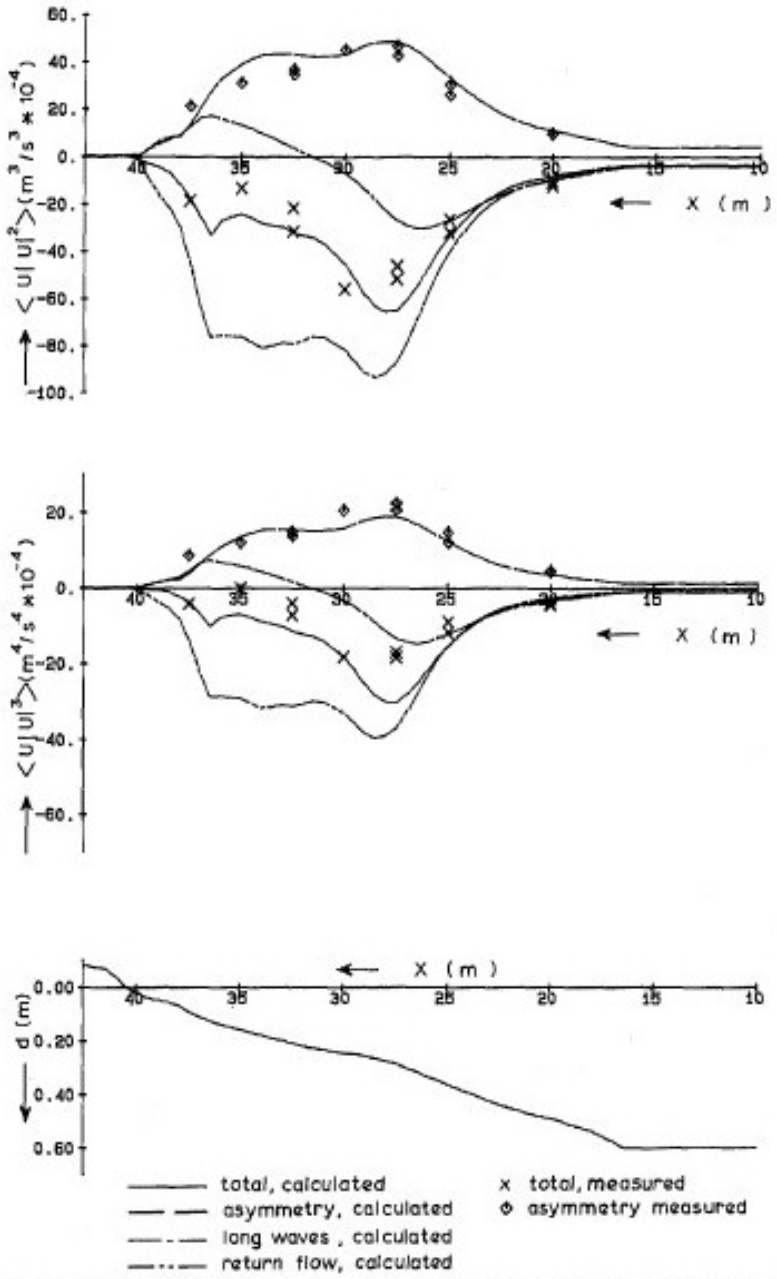

Figure 2-1: Total odd flow moments $U|U|^n$ and their constituent components; measurements (symbols) and model predictions (lines) including the effect of the undertow from Roelvink and Stive [21]

Chapter 3

Methodology

In this chapter, the methodology to compute cross-shore flows is described with regard to the numerical tool and the decomposition technique. To begin with, the properties, the governing equations and the numerical framework of the model SWASH are interpreted in section 3-1. With results obtained through SWASH, the decomposition process is essential to extract the signals with desired frequency. Thus, section 3-2 provides an introduction of the background knowledge of decomposing signals starting with Fourier Transform.

3-1 Swash

The state-of-the-art wave-flow model SWASH (Simulating WAves till SHore) applies the non-linear shallow water equations including non-hydrostatic pressure, to provide a basic principle for simulating non-hydrostatic, free surface and rotational flows. SWASH is capable of providing a robust and efficient computational modelling of wave and flow at any scale in both surf and swash zones. In the following, the properties of SWASH is described in order to gain insight into this powerful tool including validities of relevant features to onshore-offshore flows. Subsequently, the governing equations are studied to have an understanding of the solutions.

3-1-1 Properties

SWASH models coastal flows and phenomena by means of solving continuity and momentum equations. A series of simulations have been validated with experimental or analytical solutions by Zijlema et.al [29]. Generally, SWASH is capable of performing following phenomena:

- Wave transformation in coastal regions;
- Non-linear interaction between waves and wave-current interaction;
- Wave breaking, wave-induced set-up and vertical turbulent mixing; etc.

These physical phenomena are of great importance on studying the mean flow under wave trough undertow $\bar{u}$, the bound long-wave flow u_{lo} and the short-wave-induced asymmetric flow u_{hi}, which are components of the contributions to cross-shore velocity moments. Hence, the wave-flow model SWASH is adopted in this study to predict the onshore-offshore flows considering the phenomena mentioned above.

Mass and momentum are conserved at discrete level, bringing about accurate simulation of propagation of breaking waves including the energy dissipation through bores. Moreover, the non-linear wave-wave and wave-current interactions in coastal waters have already been considered in the SWASH. In general, the effects of wave components due to non-linear interactions under breaking, for instance wave asymmetry and skewness, are included in the SWASH.

Another of the most favourable features of SWASH is that, either a depth-averaged mode or a multi-layered mode could be considered in the model. The layer interfaces are defined by the bottom-fitted sigma plane. By refining the vertical resolution with sufficiently high precision(more results in the vertical direction), the modelling result of velocity profile may be approximately accurate. On the contrary, for a low vertical resolution, the amplitude dispersion would be underestimated due to lacking signals of horizontal velocity near wave crest. In this study, special attention should be paid to the vertical flow structures such as undertow. More than 10 vertical layers should be applied to produce more accurate velocity profile. In addition, the vertical turbulent dispersion is advised to be calculated by the standard k-ϵ turbulence model.

With respect to the presence of wave grouping-induced long waves in the SWASH, the option 'ADDBOUNDWAV' is adopted at the wave-maker boundary to add second order solution of incident bound long waves to the irregular waves. The formed infra-gravity waves are generated by non-linear wave-wave interactions and then propagate shoreward throughout the interesting domain [19].

In summary, SWASH can be used to describe a large amount of physical phenomena including the cross-shore flows contributing to the velocity moments. However, coastal flows are incredibly complicated and thus, the competence of SWASH to simulate cross-shore flows should be verified.

Firstly, Smit et.al [22] have concluded that SWASH is capable of resolving near-shore wave processes considering depth-induced wave breaking. Furthermore, the simulation of wave asymmetry and skewness by means of SWASH has been proved to be in good agreement with measurements for mid-energetic conditions according to Brinkkemper [10]. In addition, Rijnsdorp et.al [20] have verified the capability of SWASH in simulating the cross-shore transformation of bound and free infra-gravity waves induced by the bi-chromatic waves. For a plane sloping bottom, SWASH correctly predicts the near-shore transformation of bound long waves but a bit overestimates the magnitude of the outgoing free long waves. Nonetheless, SWASH predict overall well for the wave grouping-induced long wave flow. These cases justify that SWASH is capable of simulating most of the cross-shore flows relevant to the velocity moments mentioned above. Moreover, there is little literature with regard to the applicability of SWASH to simulate the undertow correctly. Hence the prediction of undertow is particularly analysed in the model set-up.

3-1-2 Governing Equations

The hydrodynamic model SWASH is governed by the non-linear shallow water equations derived from the three dimensional(3D) Navier-Stokes equations that describe the conservation of mass and momentum of incompressible fluid with constant density. Since the interest area of this study is in the perpendicular direction to the beach, we modify the 3D governing equations to a two-dimensional vertical (2DV) mode in Cartesian coordinate system. The 2DV plane is vertically bounded by the free surface level $z = \zeta(x,t)$ and the bottom level $z = -d(x)$ defined relative , where x and z are coordinates and t indicates the time. For more detailed interpretation of the governing equations may consult Zijlema and Stelling [28] and Zijlema et.al [29].

The 2DV governing equations are given by [22]:

$$\frac{\partial u}{\partial x} + \frac{\partial w}{\partial z} = 0 \tag{3-1}$$

$$\frac{\partial u}{\partial t} + \frac{\partial uu}{\partial x} + \frac{\partial wu}{\partial z} = -\frac{1}{\rho}\frac{\partial (p_h + p_{nh})}{\partial x} + \frac{\partial \tau_{xx}}{\partial x} + \frac{\partial \tau_{xz}}{\partial z} \tag{3-2}$$

$$\frac{\partial w}{\partial t} + \frac{\partial uw}{\partial x} + \frac{\partial ww}{\partial z} = -\frac{1}{\rho}\frac{\partial p_{nh}}{\partial z} + \frac{\partial \tau_{zz}}{\partial z} + \frac{\partial \tau_{zx}}{\partial x} \tag{3-3}$$

where, u and w are flow velocities in the x and z directions respectively, ρ indicates a constant density,p_h and p_{nh} are the hydrostatic and non-hydrostatic pressures respectively, $\tau_i j$ represent the horizontal turbulent stresses.

The equations are solved in time along horizontal direction x and vertical direction z. The first terms in the left hand side of the momentum equations Eq. (3-2) Eq. (3-3) reflect the rate of change in time along x- and z- directions, respectively. The second and third terms both represent advection. With regards to the right hand side of momentum equations, the first term indicates the pressure gradient which is divided into hydrostatic and non-hydrostatic parts. The hydrostatic pressure is formulated with the free surface elevation ζ, $p_h = \rho g(\zeta - z)$, in which $g = 9.81 m/s^2$ is the gravitational acceleration. Hence the hydrostatic pressure gradient can be expressed as its equivalent in terms of free surface level $\frac{\partial p_h}{\partial x} = \rho g \frac{\partial \zeta}{\partial x}$. The free surface elevation is computed by considering the conservation of mass over the water depth with the kinematic condition $w = \frac{\partial \zeta}{\partial t} + u\frac{\partial \zeta}{\partial x}$ using at the free surface and the final expression is given by:

$$\frac{\partial \zeta}{\partial t} + \frac{\partial}{\partial x}\int_{-d}^{\zeta} u dz = 0 \tag{3-4}$$

The remaining terms τ_{ij} of the momentum equations Eq. (3-2) Eq. (3-3) represent the turbulent stresses, with which the vertical turbulent mixing may be described by means of turbulent viscosity approximation. Furthermore, vertical eddy viscosity is considered to present the impact of bottom stress over the entire water column. With a high resolution along the vertical direction, it is recommended to adopt the standard $k - \epsilon$ turbulence model developed by Lauder and Spalding [15] to obtain the eddy viscosity.

The turbulent stresses are given by: $\tau_{xx} = 2v_h \frac{\partial u}{\partial x}$, $\tau_{xz} = v_h \frac{\partial w}{\partial x}$, $\tau_{zx} = v_v \frac{\partial u}{\partial z}$, $\tau_{zz} = v_v \frac{\partial w}{\partial z}$, where, v_h and v_v are the horizontal and vertical eddy viscosity due to wave breaking, respectively. It is advised to specify background viscosity in SWASH to solve all types of vertical turbulent mixing, a value of $10^{-4} m^2/s$ is adopted in this study.

In order to solve the governing equations Eq. (3-1)-Eq. (3-4), boundary conditions are required to be imposed at the free surface, the bottom, the wave-maker boundary and the shoreline. At the surface, the kinetic condition has been applied for obtaining free surface elevation:

$$w|_{z=\zeta} = \frac{\partial \zeta}{\partial t} + u \frac{\partial \zeta}{\partial x} \tag{3-5}$$

In addition, we assume no surface stress and hence, the dynamic surface boundary condition indicates a constant pressure:

$$p_h|_{z=\zeta} = p_{nh}|_{z=\zeta} = 0 \tag{3-6}$$

At the bottom, the kinetic condition is adopted to impose the normal velocity:

$$w|_{z=-d} = -u \frac{\partial d}{\partial x} \tag{3-7}$$

Note that the bottom friction plays a vital role in low frequency wave motions and set-up, thus a bed stress is included in the momentum equations Eq. (3-2)Eq. (3-3). As mentioned before, the interest of vertical flow structure requires high vertical resolution (>10 layers). In this case, the wall functions based on the logarithmic law of the wall are applied for either a smooth or a rough bottom. The roughness term is determined by a Nikuradse roughness height according to the SWASH user manual [26]. However, the Nikuradse roughness height for the plane bottom under oscillatory flows is sensitive to the Shields parameter due to wave oscillation [11] which cannot be easily estimated. In this study, the friction roughness coefficient is obtained through sensitivity study.

The incident waves are generated at the offshore boundary by imposing a time series of wave record or a wave spectrum. Moreover, the bound long wave is added by prescribing the horizontal velocity based on second order wave theory [20]. The moving shoreline approach is adopted at the interface between water and land to simulate the wave set-up properly [23].

3-1-3 Numerical Implementation

SWASH applies the numerical implementation on the staggered grids based on an explicit, second order accurate finite difference method both in space and time. As is known to us, the pressure is split-up into hydrostatic and non-hydrostatic parts. When considering the discretization of the vertical pressure gradient, the Keller Box or the standard central differences layout may be adopted to a case with low or relatively high vertical resolution, respectively [22]. More than 10 layers is desired in this study and thus the standard layout is employed to approximate non-hydrostatic pressure. Additionally, the non-hydrostatic pressure is included by solving the Poisson pressure equation with an iterative solution. When a multi-layered case is involved, the BiCGSTAB accelerated with the ILU pre-conditioner is applied in order to solve the Poisson equation efficiently in robust manner [26].

The momentum must be conserved in the entire computational domain for simulating wave properties under breaking waves accurately. Additionally, the advection terms in the momentum equantions (3-2) Eq. (3-3) are approximated by appropriate discretization schemes for the sake of conserving momentum. The schemes recommended by the User Manual [26], for applications where breaking and vertical flow structures are of great importance, are outlined in the Table 3-1.

Table 3-1: Discretization schemes of advection in momentum equations (CDS: Central Differences Scheme; BDF: Backward Differentiation Formula scheme; UPW: first order UPWIND scheme)

Advection Term	Numerical Schemes
Horizontal advetion term of u-momentum $\frac{\partial uu}{\partial x}$	CDS or BDF(default)
Horizontal advetion term of w-momentum $\frac{\partial uw}{\partial x}$	CDS or BDF(default)
Vertical advetion term of u-momentum $\frac{\partial wu}{\partial z}$	CDS or UPW(default)
Vertical advetion term of w-momentum $\frac{\partial ww}{\partial z}$	UPW(default)

The application of moving shorelines requires non-negative water depth and the mass conservation approximated by first order upwind scheme [23]. The model considers the velocities as zero when the water depth is smaller than a threshold value set by the user. Moreover, the water depth in velocity points is obtained by interpolation which would result in unexpected errors. If a second order accuracy is desired, a flux limiter may be adopted to get a higher order interpolation. Consequently, the discretization for the water depth in velocity points will be considered and calibrated in the model.

For computational efficiency, the time integration employs an explicit scheme. So the well-known CFL condition is considered to restrict the time step in order to get stable solutions. The CFL condition is given by an expression in terms of Courant number:

$$C_r = \frac{\Delta t(\sqrt{gd} + u)}{\Delta x} \leq 1 \tag{3-8}$$

where, C_r is the Courant number,$\sqrt{gd}$ indicates the wave group speed, u represents the velocity, Δt and Δx are the time and spatial step, respectively. With this equation, the time step is adjusted dynamically based on the Courant number within a predefined range $C_{r_{min}} \leq C_r \leq C_{r_{max}}$. The maximum Courant number $C_{r_{max}}$ is set to 0.5 in case of high harmonics and nonlinearies while the minimum value $C_{r_{min}}$ of 0.1 is selected. With regards to the time integration of vertical terms, the default second order Crank-Nicolson scheme($\theta = 0.5$, with θ the weight parameter between explicit and implicit Euler schemes) is adopted.

3-2 Decomposition Technique

The model output of SWASH is usually a record as a function of time. As an example, a time series of surface elevation are shown in the Figure 3-1. In order to obtain different wave components in terms of frequency, a method to transform the signal from time to frequency domain is required. The most commonly used approach is Fourier transforming the time series of wave records to the frequency signals directly with the numerical Fast Fourier transform (FFT) algorithms. In this section, the decomposition technique is organized by the basic knowledge of Fourier Transform and FFT with an application, and a description of the filter used to decompose signals with different frequencies.

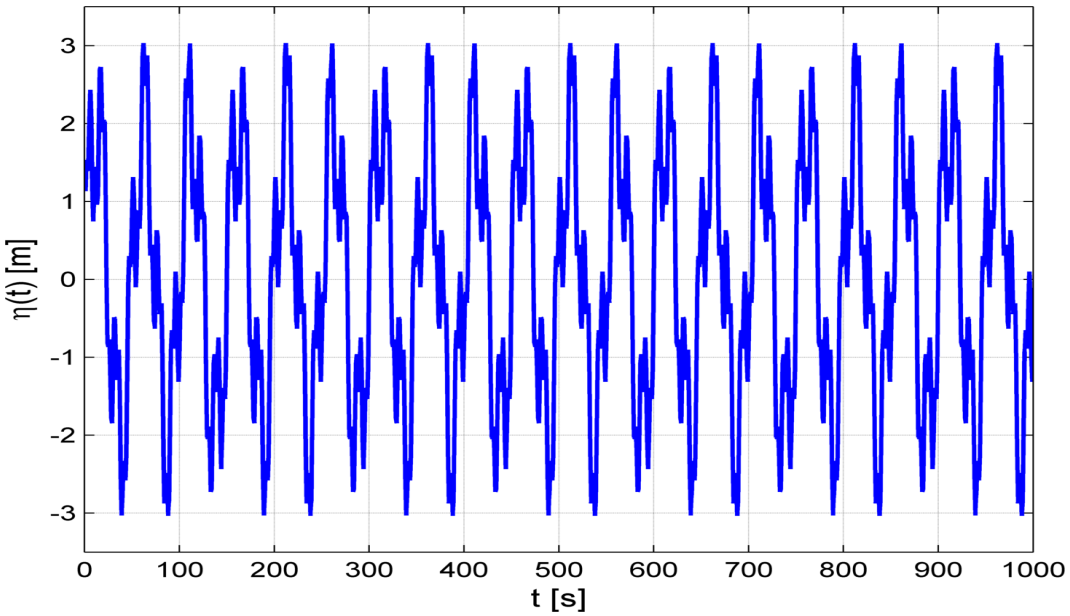

Figure 3-1: Signal of surface elevation synthesized with a time series

3-2-1 Fourier Transform

Fourier transform is widely used to obtain the signals in the frequency domain starting from a time series of records. It is essential to understand the inherent principle as well as the equations of Fourier transform to make sure that the transformation is processed in a correct manner.

The Fourier analysis begins with the periodic signal represented by the Fourier series with unknown amplitudes a_i and phases α_i [13]:

$$x(t) = \sum_{i=1}^{N} a_i cos(2\pi f_i t + \alpha_i) \qquad with f_i = \frac{i}{D} \tag{3-9}$$

where i is the sequence number in the signal record, D is the duration of the record and f_i is the frequency of component i.

The trigonometric Fourier series may be rewritten as:

$$x(t) = \sum_{i=1}^{N} [A_i cos(2\pi f_i t) + B_i sin(2\pi f_i t)] \tag{3-10}$$

with,

$$a_i = \sqrt{A_i^2 + B_i^2} \tag{3-11}$$

$$\alpha_i = -\frac{B_i}{A_i} \tag{3-12}$$

The Fourier coefficients A_i and B_i can be derived by integrating the series of wave record, based on the trigonometric identities:

$$A_i = \frac{2}{D} \int_D x(t) cos(2\pi f_i t) dt \qquad for f_i = \frac{i}{D} \tag{3-13}$$

$$B_i = \frac{2}{D} \int_D x(t) sin(2\pi f_i t) dt \qquad for f_i = \frac{i}{D} \tag{3-14}$$

With the Fourier coefficients, the amplitudes a_i and phases α_i can be computed by Eq. (3-11) and Eq. (3-12). In this manner, all the wave components can be obtained and subsequently the expectation $E\{\frac{1}{2}\underline{a}^2\}$. Theoretically, the variance density spectrum can be obtained by means of distributing the expectation $E\{\frac{1}{2}\underline{a}^2\}$ over the frequency interval Δf and then take the limit of the frequency interval to zero to achieve a continuous spectrum which is defined as:

$$E(f) = \lim_{\Delta f \to 0} \frac{1}{\Delta f} E\{\frac{1}{2}\underline{a}^2\} \tag{3-15}$$

When considering the frequency interval to approach zero, the duration of the signal goes to infinity and hence, the analysis of Fourier series is extended to the Fourier transform. For convenient reasons, the Fourier series can be written as complex exponential functions by means of Euler's formula:

$$x(t) = \sum_{n=-\infty}^{\infty} X_i e^{j2\pi f_i t} \tag{3-16}$$

with,

$$X_i = \frac{1}{D} \int_{-\frac{D}{2}}^{\frac{D}{2}} x(t) e^{-j2\pi f_i t} dt \tag{3-17}$$

By taking the limiting process $D \to \infty$, a continuous-time signal can be expressed by the Fourier transform:

$$X(f) = \int_{-\infty}^{\infty} x(t) e^{-j2\pi f_i t} dt \tag{3-18}$$

However, the outputs obtained from the model are discrete with a fixed time interval, our attention should be turn to Discrete Fourier Transform (DFT). The sampling theorem is therefore applied here and the integral in the Eq. (3-18) is considered to be replaced by discrete sum:

$$X_s(f) = \sum_{n=1}^{N} x(n\Delta t)e^{-j2\pi fn\Delta t} \tag{3-19}$$

To achieve the digital computation for Eq. (3-18), the frequency should be discretized into a series of values as 0, 1/D,...,(N-1)/T. The frequency f is defined as $f = \frac{k}{T}$ for the sake of efficiency. The resulting expression of the Fourier transform of the discrete-time signal is given by:

$$X_k = \sum_{n=1}^{N} x(n)e^{-j2\pi(k-1)(n-1)/N} \qquad k = 0, 1, ..., N-1 \tag{3-20}$$

In practice, this summation is usually approximated by the Fast Fourier transform(FFT) algorithm for efficient reason. For a set of N samples, $4N(N-1)$ real multiplications are required to compute all the output points, while the FFT algorithm only needs $2Nlog_2N$ real multiplications. Hence, the FFT algorithm is applied to achieve the discrete Fourier transform in this study.

According to the sampling theorem, the sample rate f_s should be sufficient to reconstruct the continuous signal from a sequence of discrete samples by means interpolation. To ensure a high fidelity of the signal, the sample rate must be large enough to distinguish the component of maximum frequency from the waves of low frequencies. Otherwise, the spectrum of high frequencies are mirrored around the so-called Nyquist frequency [13]. In other words, the components with frequencies above the Nyquist frequency are not distinguishable and the energy densities of relatively high frequencies may be added to the energy densities of low frequencies, resulting in an aliasing phenomenon.

The Nyquist frequency can be computed by Eq. (3-21):

$$f_{Nyquist} = \frac{1}{2\Delta t} \tag{3-21}$$

in which, Δt is the discrete time interval, $\Delta t = \frac{1}{f_s}$. It is obvious that the Nyquist frequency is half of the sample rate f_s.

To ensure no wave component is missed out during the sampling process, the Nyquist frequency must be larger than the maximum component frequency to avoid aliasing, i.e. the sample rate f_s is at least twice the maximum frequency of the wave record. In the practice of waves in the coastal water, it is advised to choose a value of Nyquist frequency higher than a characteristic frequency of the wave spectrum instead of the maximum frequency. This is because the wave energy densities in the tail are relatively small and thus might be regardless. Holthuijsen [13] suggested to adopt four or five times the mean frequency as the Nyquist frequency. The time interval Δt for the outputs is therefore set according to the Nyquist frequency.

With the knowledge of Fourier transform, the signal of surface elevation which is shown in the Figure 3-1 can be studied through applying the FFT algorithm to get the density spectrum

for wave analysis. The duration of the signal is 1000 s and the sample rate is set to 1 Hz, hence there are 1000 samples of the signal. The variance density spectrum demonstrated in the Figure 3-2 is acquired through the MATLAB fft function.

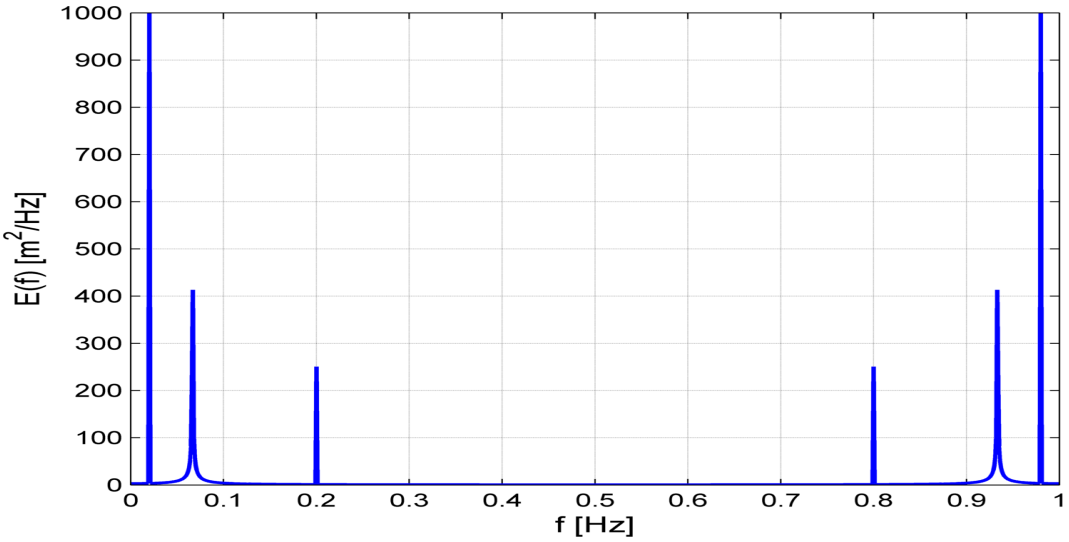

Figure 3-2: Signal of variance density spectrum

It can be read from the Figure 3-2 that the signal contains 3 components of frequencies of 0.02, 0.067 and 0.2, respectively. The Nyquist frequency is 0.5 Hz where the energy densities are mirrored around, this fulfil the Nyquist Criterion that the maximum frequency of the signals is smaller than the Nyquist frequency.

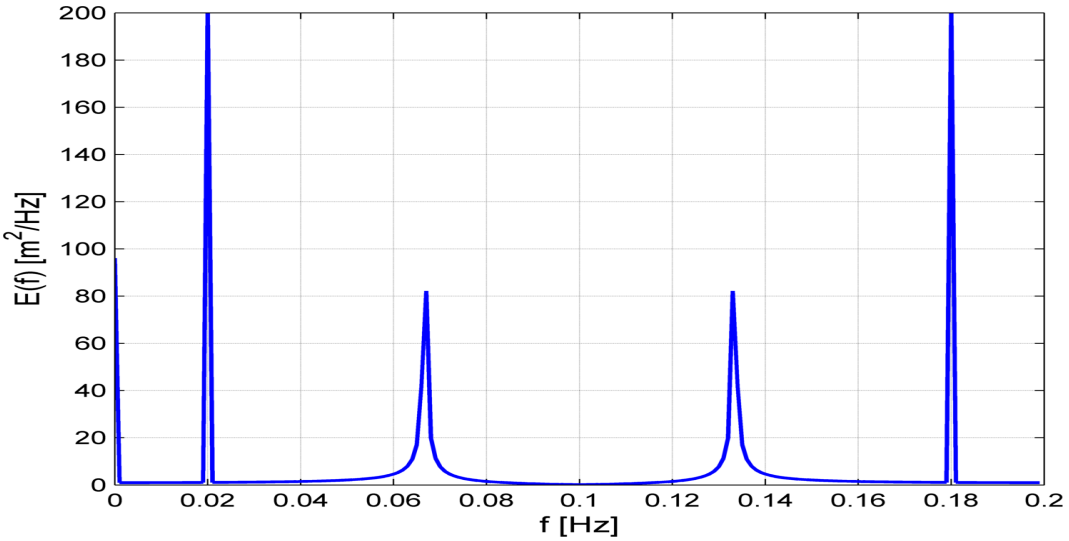

Figure 3-3: Aliasing in variance density spectrum

An example of the aliasing is shown in the Figure 3-3, it is achieved by choosing a sampling rate $f_s = 0.2$Hz which is smaller than twice the maximum frequency. As can be seen in the Figure 3-3 that, the component with frequency higher than the Nyquist frequency $f_Nyquist = 0.1$Hz is not exhibited. Its frequency (f=0.2 Hz) is too high to be discerned by a Nyquist

frequency of 0.1 Hz and hence, its information is lost after the Fourier transform.

The further application of the obtained spectrum is introduced with the filter, with which the signal with desired frequency can be extracted.

3-2-2 Filter

From the Figure 3-2, high and low waves can be easily distinguished in terms of frequency. Suppose we are interesting in the component with the frequency smaller than 0.05 Hz, the desired signal can be obtained by the filter which simply zeros out the energy densities of frequencies larger than 0.05 Hz. Since the spectrum was mirrored around the Nyquist frequency, the copied signal at the other side (f>0.95 Hz)should be preserved as well. After that, the inverse fast Fourier transform (IFFT) is applied to get back the time series of surface elevation of low frequency wave(<0.05 Hz) shown in Figure 3-4.

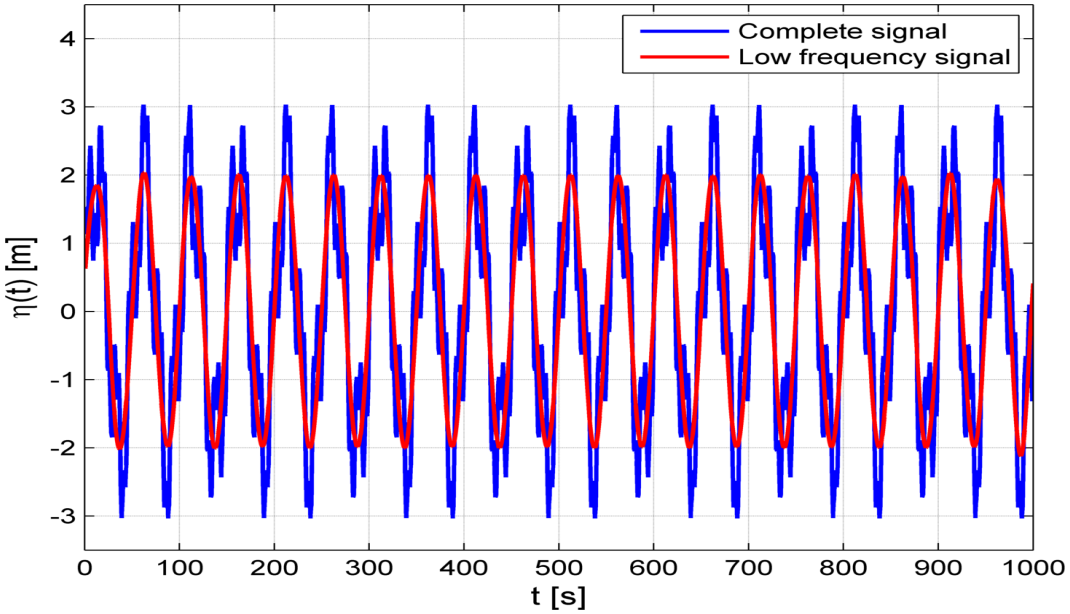

Figure 3-4: Signal of low frequency extracted by fast Fourier transform

This Figure indicates that the amplitude of low frequency wave(<0.05 Hz) is about 2 m. The result may be checked by a simple calculation: $Amplitude = E(f) * 2/N$, in which N is the number of the samples and is therefore 1000 in this case. The amplitude of the low frequency wave is therefore $Amplitude = 1000 * 2/1000 = 2m$, corresponding to the amplitude indicated in Figure 3-4.

Chapter 4

Application for Wave Flume Case

It is essential to have a validation with a set of measurements to make sure that the method introduced in Chapter 3 is executable to calculate the contributions to onshore-offshore velocity moments. In this chapter, the non-hydrostatic model SWASH is setup and investigated by means of sensitivity study to determine the optimal settings.

4-1 Wave Flume Experiment

Roelvink and Stive [21] implemented an experiment in a wave flume, with a length of 55m, a width of 1m and a height of 1m, at Delft Hydraulic(now Deltares). Two bottom profiles were built up: one was a initially plane beach with a slope 1:40 and the other was a beach with a single bar with the same slope. These configurations both represent a surf zone with dissipative beach. The beach was made of medium to fine quarts sediment with a median grain size of 100 μm.

The experiments were performed with random, grouped waves which were generated by using a piston-type wave board on a water depth of 0.60 m approximately. In order to prevent the reflection of outgoing free long waves at the wave board(re-reflection), active wave absorption was applied at the wave generator [14]. The random waves were created as JONSWAP type and the peak enhancement parameter γ was set as 3.3, which is the average value of γ based on JONSWAP study at various locations and times [13]. For measuring instrument, the surface elevation were measured by wave gauges and the near bottom flow was measured at 0.05 m above bottom by Acoustic Sediment Transport Meter(ASTM).

Three tests were considered on the two bottom profiles mentioned above with different wave conditions. A summary of bottom configurations and wave parameters imposed at the boundary for every test is presented in the Table 4-1. As can be seen that, three tests was conducted with different wave conditions of normal, low and high wave steepness respectively.

In this project, the odd velocity moment in the cross-shore direction are separated into the velocity moment related to the mean flow velocity $< \bar{u}|u_{hi}|^2 >$, the velocity moment due to

Table 4-1: Bottom profile and wave conditions for experiment tests

Test	Bottom Profile	H_{rms}[m]	f_p[Hz]	Durations [Hour]
1	plane slope	0.123	0.5	12
2a	single bar slope	0.081	0.5	12
2b	single bar slope	0.133	0.5	12

the short wave asymmetry $< u_{hi}|u_{hi}|^2 >$ and correlation between the long wave forced by the wave group and short wave velocity variance $< u_{lo}|u_{hi}|^2 >$. Hence it is vital to study the undertow(mean current), infra-gravity waves and short wave properly. The wave breaking is therefore of utmost importance.

In the test 1, waves of normal steepness transmitted on the sloping plane beach (1:40) for 12 hours. The wave breaking approximately occurred at the middle of flume according to the wave steepness. In the test 2a, 12 hours of waves of a relatively small steepness was performed on the sloping beach (1:40) with a single bar. The wave condition was so mild that the breaking area was too shoreward, the breaking area was so shallow that the results were not reliable. Test 2b was executed on the same bottom profile and duration as test 2a but with a incident wave of much higher wave steepness. The wave breaking was observed before the single bar, it was a little offshore so that the result were not representative. Thus, we will reproduce the test 1 by applying non-linear numerical model SWASH in the following section, the relevant topography is illustrated in Figure 4-1

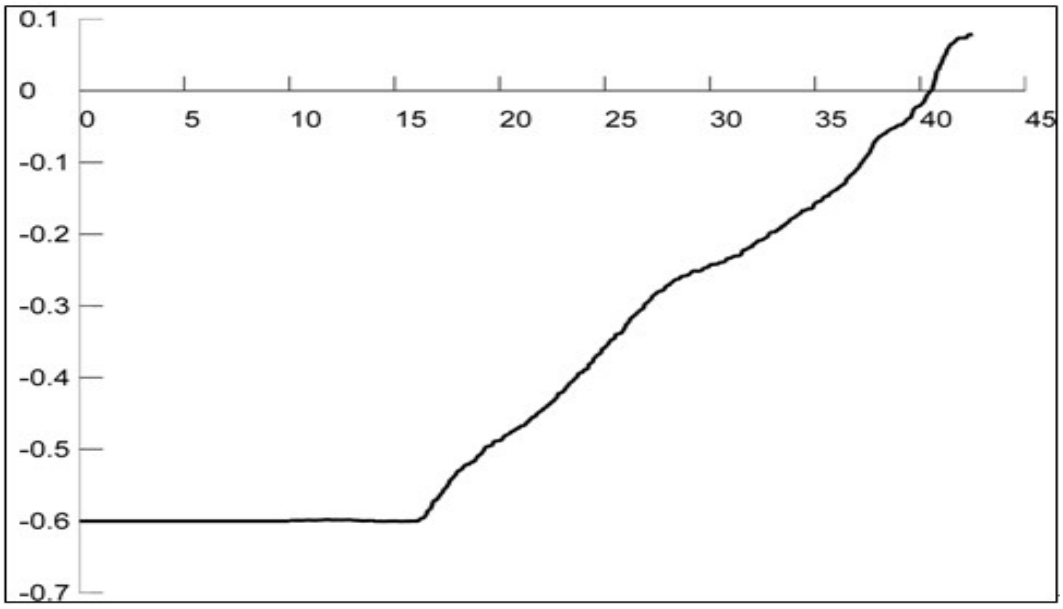

Figure 4-1: Topography for test 1

4-2 Model Setup

In order to reproduce the contributions to the cross-shore velocity moments by using SWASH, the effects of undertow, bound long waves and wave asymmetry should be investigated beforehand. In the following, the necessary numerical solutions of SWASH used to describe these effects are discussed. Furthermore, the detailed settings of all the simulations carried out in this study, are demonstrated term by term.

The undertow is a wave-induced mean current below the wave trough in case of wave breaking. This wave-averaged flow is a compensation for the balance between the horizontal gradient of the radiation stress and the wave set-up-induced pressure gradient. Additionally, wave breaking induced turbulence also affects the undertow in the surf zone. However, the SWASH is not implemented with the turbulence generated by the breaking yet which will be discussed with the results. Furthermore, a simple approach to consider the wave grouping-induced long waves in the SWASH is adding bound long waves at the wavemaker boundary, while the wave asymmetry and skewness are preserved in the model without any specification. Consequently, the numerical solutions of wave height, water set-up, mean velocity and total velocity are required to calculate the undertow, the long wave flow and the asymmetric flow.

4-2-1 Computational Grid

A two-dimensional vertical(2DV) mode was considered to simulate the flume experiment test 1 using SWASH in the Cartesian coordinates system. The horizontal grid resolution was 0.05 m, which was determined by the requirement of 50-100 grid cells per wave length associating with peak wave frequency according to the linear dispersion relation. When modelling the wave propagation, such as the wave height, 10 layers was sufficient to obtain accurate result avoiding the setting of wave breaking. However, in the case of simulating undertow and flow velocity, the number of layers was set to 20, 30 and 40 respectively, in order to have sufficient resolution for the velocity profile. Both equivalent and varied distributions of the vertical resolution were considered in the model.

4-2-2 Boundary Conditions

The imposition of boundary condition should be correct and robust in order to solve the governing equations accurately. Simply note that the initial condition was set to zero since the experiment started with constant water level and zero velocity. Based on the description of the laboratory test 1, a JONSWAP spectrum with a peak enhancement factor of 3.3 was exerted and the measured surface elevation density spectrum at x=10m which is shown in a dimensionless smoothed form in the Figure 4-2.

There were two kind of methods applied in this study to define the spectrum at the boundary. One specified the wave spectrum with the spectral parameters, namely the characteristic wave height, the characteristic wave period, the peak wave direction, the directional spreading coefficient and the cycle period. The other imposition was defined by means of creating a file containing the wave spectrum measured at x=10m with the cycle period as well. The cycle period indicated the time period over which the surface elevation and the velocities are synthesized, it should be long enough to obtain reasonably reliable solutions. However, the

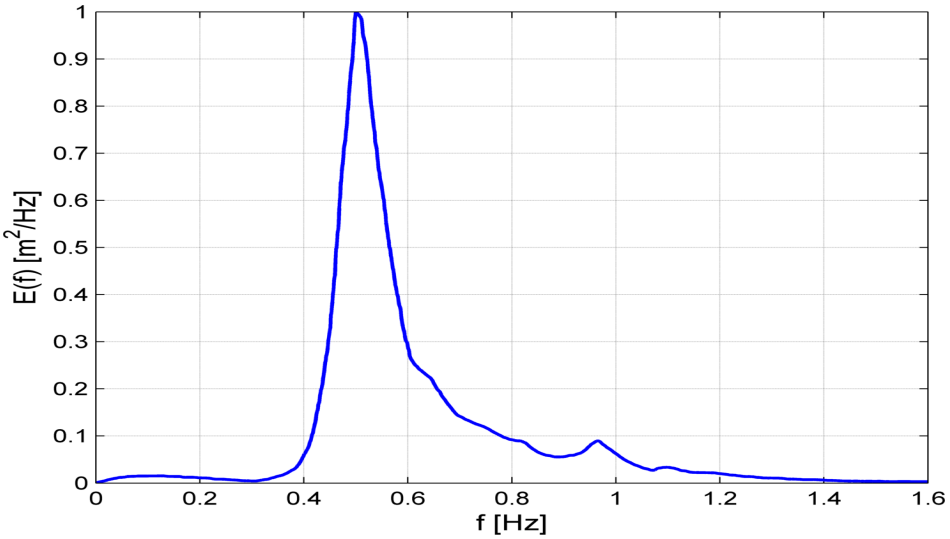

Figure 4-2: Dimensionless smoothed surface density spectrum measured at x=10m

longer the duration, the more wave components will be generated at the offshore boundary which would result in non-stationary. Here, the cycle period of surface elevation and velocities to be synthesized was set to 15, 30, 40 minutes, respectively. Nevertheless, for the simulation of imposing spectrum file at x=10m, a relatively small frequency interval is not applicable in SWASH yet. The cycle period is defined as the inverse of frequency interval, only a relatively short cycle period of 1000 seconds was adopted in this case.

In the laboratory case, the active wave absorption was employed to prevent the reflection of the offshore directed free long waves. To achieve this aim, a weakly reflective condition was adopted to avoid the re-reflection at the wave-maker boundary. Moreover, the bound long waves were incorporated in SWASH by adding a second order solution to the primary wave. Since the wave grouping-induced long wave flow plays a relatively vital role in this study, it is favourable to gain insight into this model setting by means of sensitivity analysis between the cases with and without adding bound long waves at the offshore boundary.

With respect to the boundary at the shoreline, no boundary condition was specified. In this case, the boundary represented a fully reflective and dissipative beach in accordance with the experiment setup.

4-2-3 Physical and Numerical Parameters

The bottom friction may play a dominant role in a case involving long waves and return current. As mentioned above, the Nikuradse roughness height was employed to consider the bottom friction in the model. A number of models to study the Nikuradse roughness height have been developed but it remains difficult to select the optimum. Moreover, most of the models indicate that the roughness height depends on the characteristic grain size and the Shields parameter. However, the latter term is not easy to be determined. In this case, a simple formula without the Shields parameter was desired to get an approximate value, and then the friction roughness coefficient was obtained through the sensitivity study.

Camenen [11] summarized several formulas to compute the Nikuradse roughness height and the relationship proposed by Madsen(1993) was chosen since the Shields parameter was not accounted for:

$$\frac{k_s}{d_{50}} = 15 \tag{4-1}$$

where, k_s is the Nikuradse roughness height, d_{50} is the median grain diameter.

In the laboratory case, the bottom was comprised of medium to fine sediment of a median grain diameter of 100 μm. Hence the roughness height was set to 0.0015 m. Based on this value, SWASH employed the Nikuradse roughness height of 0.0015 m, 0.003 m and 0.005 m respectively to get the proper setting for bottom friction.

Since the vertical flow structure is of utmost importance to study near-bottom flows, the vertical turbulent mixing was therefore modelled by using the well-known k-ϵ model. The background viscosity was set to $10^{-4} m^2/s$ for the sake of stability.

With respect to the wave breaking, 10-40 layers were sufficient to describe the velocity profile as well as the breaking-induced dissipation. Hence nothing had to be specified regarding wave breaking in this study. Additionally, the command BREAK to control the wave breaking in a case with relatively coarse vertical solution was still studied and an example of using BREAK incorrectly in a case of sufficient layers was demonstrated as well, see Appendix B.

The vertical pressure gradient was discretized by the standard central differencing and the non-hydrostatic pressure was included in the non-linear shallow water equations by means of solving Poisson pressure equation accelerated with ILU pre-conditioner. Moreover, in order to simulate the wave phenomena under breaking waves accurately, the momentum must be conserved. In this manner the energy dissipation was therefore captured. Based on the Table 3-1, there are 8 set of numerical schemes for the discretization of the advection terms in the momentum equations which are appropriate to simulate vertical flow structure. All the combinations were adopted in sensitivity analysis to find the optimal setting. Furthermore, the moving shoreline approach was achieved by ensuring non-negative water depths and applying a first order upwind scheme to the global continuity equation. In addition, to gain more insight into the discretization of water depth in velocity points, a sensitivity study was conducted among first order upwind scheme, central difference scheme and a second order interpolation augmented with MUSCL flux limiter.

The initial time step was set as 0.006 s with a maximum Courant number of 0.5 to enable stable simulations. The duration comprised both the spin-up time and the time period over which the reliable data was outputted under steady-state condition. The spin-up time is defined as the time taken up to eliminate the influence of the initial condition on the model results. In this case the spin-up time was chosen as 20 minutes and the time period to reach the steady-state condition was approximated as 30 minutes. Consequently, the duration was set as 1 hour to ensure a steady-state condition.

As can be seen in the Figure 4-2 that the maximum frequency is about 1.6 Hz and the Nyquist frequency should be larger than it. As a result, the output time interval Δt must be smaller than 0.3125 s base on Eq. (3-21). However, longer computational time is required in a case of smaller time interval. Compromising with efficiency, a time interval of 0.3 s was therefore chosen.

4-3 Sensitivity Analysis

Since a considerable number of parameters and schemes were taken into account in the model set-up, sensitivity study was essential to obtain the optimal settings in SWASH for the simulations of wave propagation and vertical flow structures. Here, the sensitivity studies were performed with two parts: one presented the simulations considering the wave decay while the other demonstrated the simulations treating the vertical distribution of velocities. In this section, the model results were compared by changing the input parameters and the numerical schemes, namely the vertical resolution, the boundary condition, the imposition of bound long waves, the friction coefficient and the numerical schemes for discretizing the advection terms and water depth in velocity points. For each case, the impact of a varying parameter or scheme on the root-mean-square wave height, the water set-up and the mean velocity at 5 cm above the bottom were assessed, which were compared to the measurements of wave flume experiment mentioned in the section 4-1. Note that, here the study of undertow was represented by the mean velocity at 5 cm above the bottom rather than the mean velocity under wave trough due to the limitation of the measuring instrument.

In the case of simulating wave decay, the baseline model was simulated with the following settings. The number of the layers was set to 20 and the boundary condition was specified with the spectral parameters as well as the imposition of bound long waves at the wave-maker boundary in a cycle period of 30 minutes. The bottom was rough described by the Nikuradse roughness height, here the value was chosen as 0.005 m. The Backward Differentiation Formula (BDF) scheme was applied to approximate the horizontal advection terms while the vertical advection terms were discretized by means of central difference scheme (CDS) and first order upwind scheme (UPW), respectively, for u-momentum equation Eq. (3-2) and v-momentum equation Eq. (3-3). Last but not least, the discretization of the water depth in velocity points was done with the default MUSCL flux limiter to achieve a second order accuracy.

The modelling settings for the simulation of vertical flow structures were almost the same as indicated above. But we chose 30 layers and the water depth in velocity points were approximated by means of first order upwind scheme (UPW) since the results were more reasonable which would be discussed in the following subsection 4-3-6.

4-3-1 Vertical Resolution

Since 20 layers is sufficient to describe the wave height and set-up accurately, no analysis was carried out for this part. In contrast, the number of layers might be of great importance to the vertical flow structures, because finer resolution may lead to more reliable prediction of the flow structure. In other word, there are more points to illustrate the velocity profile and hence the simulation is more accurate. In this case the number of layers was set to 20, 30 and 40 respectively, in order to have sufficient resolution for the accurate velocity profile. Both equivalent and varied distributions of the vertical resolution were considered in the sensitivity analysis.

As can be seen in the Figure 4-3 that, the horizontal axis represents the distance from the position of wave-generator to the shoreline (left to right) while the vertical axis indicates the mean velocity at 5 cm above the rough bottom. The solid and dashed black lines illustrate

the results solved by Roelvink and Stive [21] with and without lag, respectively. The lag is a value to describe the dissipation of the turbulent kinetic energy lagging behind the production term. The blue stars present the measurement obtained by Roelvink and Stive [21] while the red, green, blue and orange solid lines show the results of SWASH with 20, 30, 40 equivalent and 30 differently distributed layers, respectively. Note that the predictions of SWASH were averaged over 8 seconds.

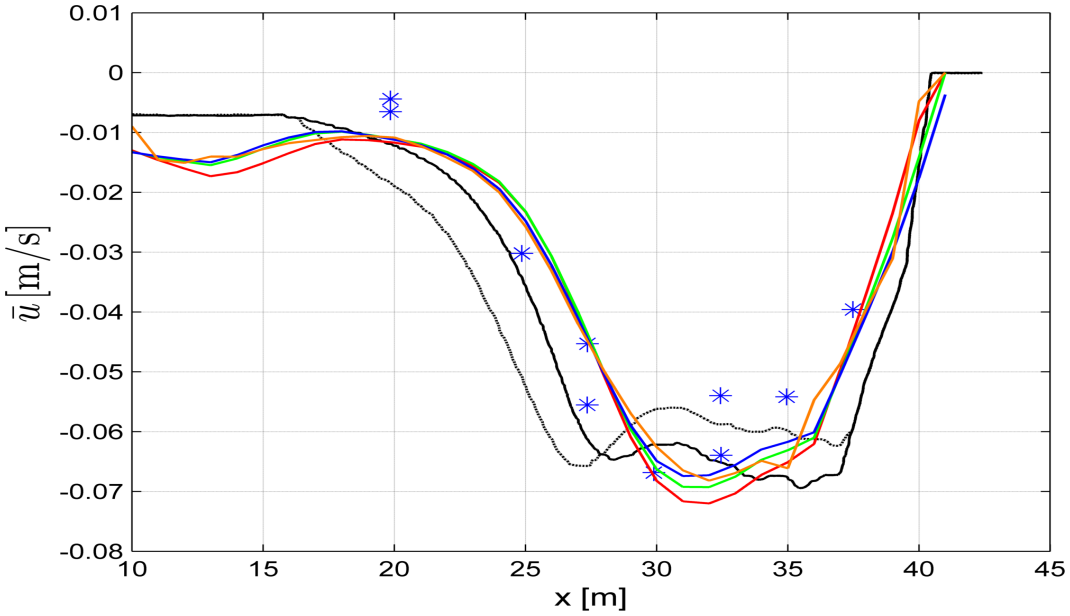

Figure 4-3: Mean velocity at 5 cm above bottom with varied vertical resolution. Roelvink and Stive with lag(black solid line), Roelvink and Stive without lag(black dashed line), measurements(blue stars), 20 equivalent layers(red line), 30 equivalent layers(green line), 40 equivalent layers(blue line), 30 differently distributed layers(orange line).

The figure indicates that, finer resolution results in more accurate prediction but the sensitivity of different distribution of layers is not significant when sufficient resolution involved. Four cases illustrated above are compared to the measurement in Figure 4-4, in which the black line represents that the predicted result equals the measurement. The horizontal axis demonstrates the mean velocity measured at 5 cm above bottom and the vertical axis shows the mean velocity predicted by SWASH at the same position.

The result of each case versus the measurement is distributed around the black line ($\bar{u}_s = \bar{u}_m$). It is obvious that the cases with 30, 40 equivalent and 30 differently distributed layers have similar results while the case of 20 equivalent layers is relatively deviating around mean velocity smaller than -0.05 m/s. In addition, the relevant coefficient of determination and the root-mean-square error between the prediction and measurement are computed for every case to present how accurate the simulation is, see Table 4-2.

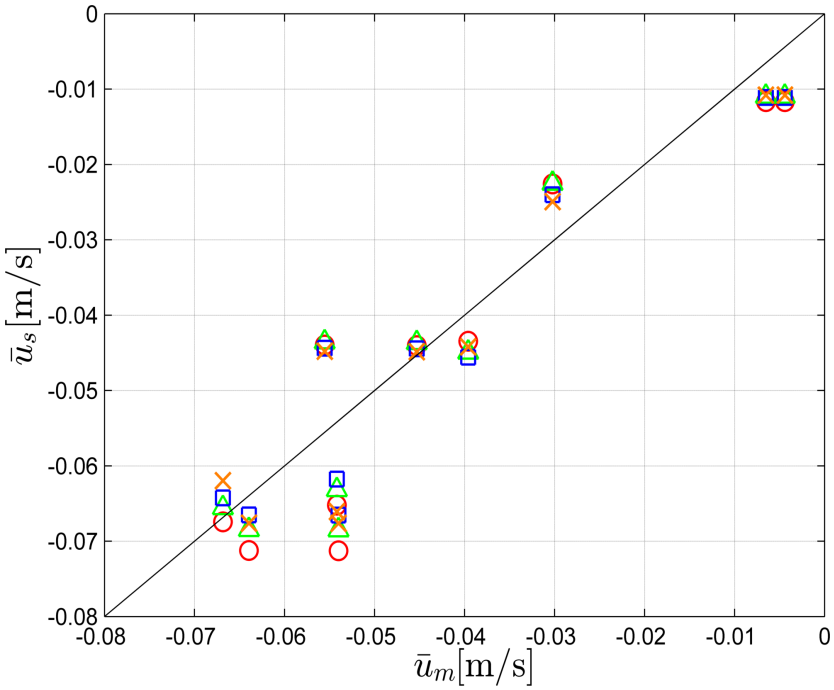

Figure 4-4: SWASH prediction versus measurement of mean velocity at 5 cm above bottom. 20 equivalent layers(red circles), 30 equivalent layers(green triangles), 40 equivalent layers(blue squares), 30 differently distributed layers(orange crosses).

Table 4-2: Coefficient of determination R^2 and root-mean-square error of mean velocity at 5 cm above bottom computed by SWASH with varied number of layers comparing to the measurement

Case	Number of layers	Distribution	R^2	Root-mean-square error
A1	20	Equivalent	0.8273	0.0087
A2	30	Equivalent	0.8614	0.0078
A3	40	Equivalent	0.8881	0.0070
A4	30	Different	0.8650	0.0077

As can be seen in the table that, the coefficient of determination for case A1 with 20 layers is much smaller than the other 3 cases. Note that, the coefficient of determination closes 1 represents that the predicted results are more close to the measurements. At the other hand, case A1 has the largest root-mean-square error among 4 cases while the case A3 with 40 layers has the smallest value. Hence, coarser vertical resolution may result in bigger error of simulation. Furthermore, both the coefficient of determination and root-mean-square error of case A2 and A4 are almost the same which shows that, the simulation is not so sensitive to different distribution of vertical layers.

In conclusion, an increase in number of vertical layers gives more accurate prediction of vertical flow structures. However, a finer resolution means a longer computation time, a compromise between accuracy and efficiency should be reached. Moreover, the vertical resolution is fine enough so that the different distributed layers is not necessarily considered in this case. For both accurate and efficient reasons, 30 equivalent layers was chosen for further analysis, providing sufficient vertical resolution for accurate simulation.

4-3-2 Imposition of Bound long waves

As indicated above, the bound long waves are incorporated in SWASH by adding a second order solution to the primary waves. A sensitivity study of the imposition of bound long waves at the offshore boundary was carried out to demonstrate the influence of adding the second order bound long waves. To gain an insight of adding bound long waves in a straightforward manner, the surface spectral density and its propagation are interpreted firstly. The density spectra were calculated by means of Fourier transform with smoothing algorithm, in order to remove noise or periodic components. Then the sensitivity of this imposition to the wave height, set-up and mean velocity at 5 cm above the bottom are discussed subsequently.

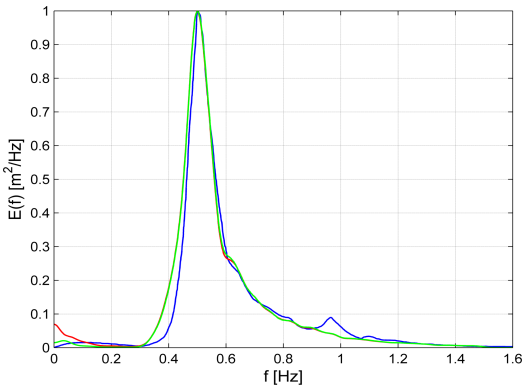

(a) Surface density spectrum at x=10m

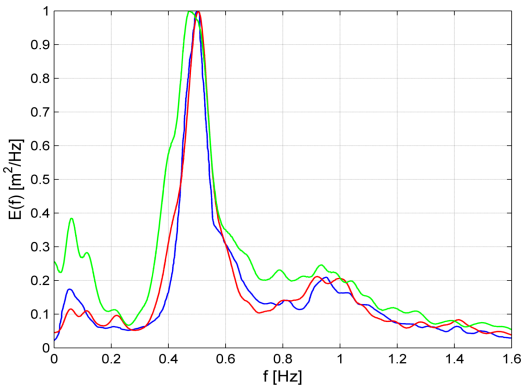

(b) Surface density spectrum at x=30.7m

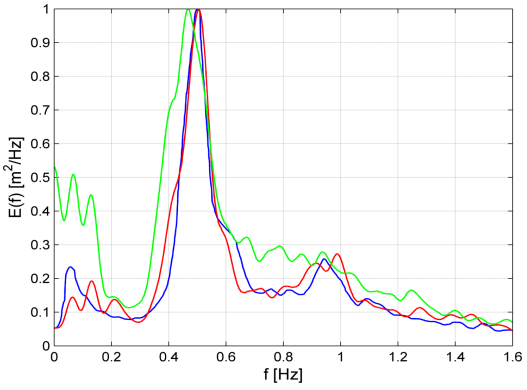

(c) Surface density spectrum at x=32.5m

Figure 4-5: Dimensionless smoothed surface density spectrum at wave maker boundary(x=10m) and in the surf zone(x=30.7m and x=32.5m) with and without adding bound long waves. Measurement(blue line), with adding bound long waves(red line) and without adding bound long waves(green line).

In the Figure 4-5, the horizontal axes represent the frequency while the vertical axes indicate the surface spectral density. The blue lines show the measurement of elevation density spectrum obtained by Roelvink and Stive[21] and the red and green lines demonstrate the results predicted by SWASH with and without bound long waves, respectively.

Figure 4-5a shows the density spectrum at the wave-maker boundary, the spectral densities of two predictions almost cover each other when the frequency is larger than 0.2 Hz. In the low frequency range(smaller than 0.2 Hz), the case with adding bound long waves shows a

larger spectral density, representing more long wave information at the offshore boundary. The difference can be explained by the imposition of second order bound long waves. Furthermore, the surface density spectra in the surf zone are illustrated in Figure 4-5b and Figure 4-5c, relatively obvious distinctions between the cases with and without adding bound long waves can be found, especially in the low frequency area. The case including bound long waves is much more accurate than the case without this imposition comparing to the measurement. As can be seen in Figure 4-5b and Figure 4-5c that, the spectral density without adding bound long wave in the surf zone are much overestimated, maybe it is due to the involvement of vertical turbulent mixing. In general, with adding second order bound long waves to the boundary condition, SWASH is capable of simulating the surface elevation correctly.

Even though the necessary of adding bound long waves to the boundary condition has been proved, it is still worthwhile to look at its influence on the wave decay and vertical velocity. In the following, the sensitivities to wave height, water set-up and mean velocity are studied with Figure 4-6 and Figure 4-8.

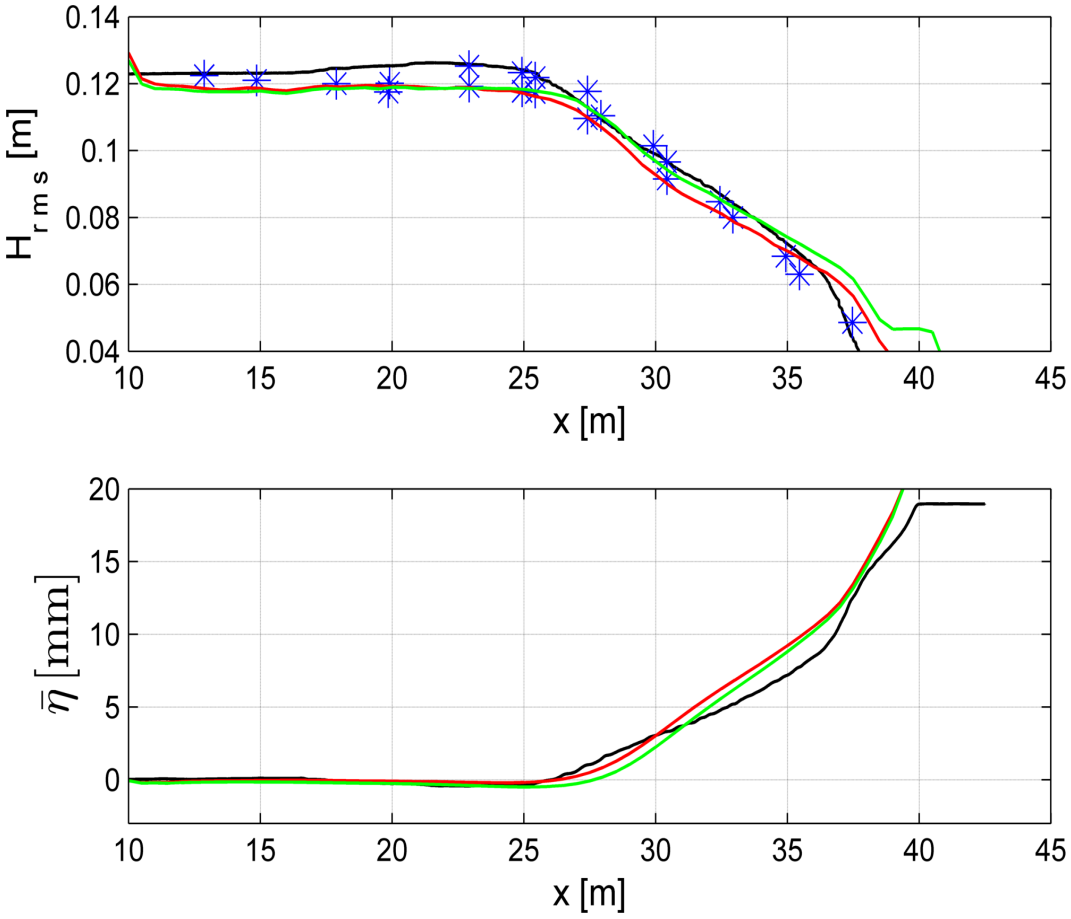

Figure 4-6: Root-mean-square wave height(upper panel) and mean water level set-up(lower panel) along the wave flume with and without adding bound long waves. Roelvink and Stive (black line), measurements(blue stars), with adding bound long waves(red line) and without adding bound long waves(green line).

Figure 4-6 illustrates the predictions of wave propagation in the surf zone. The horizontal axis indicates the distance from wave-maker boundary to the shoreline (left to right) while the vertical axes represent the root-mean-square wave height (upper panel)and water set-up(lower panel), respectively. The black lines illustrate the results solved by Roelvink and Stive [21] while the blue stars present the measurement obtained by Roelvink and Stive [21] as well. The red and green lines show the results calculated by SWASH with and without bound long waves, respectively.

The predictions of root-mean-square wave height and set-up are not sensitive to the imposition of bound long waves, which is shown in Figure 4-6. However, the case without adding bound long waves shows a slightly large error near the shoreline. It might be explained by the application of vertical turbulent mixing since many studies, e.g. Rijnsdorp[18], have proved that SWASH was capable of predicting the characteristic wave height accurately even though the SWASH was not incorporate with the bound long waves.

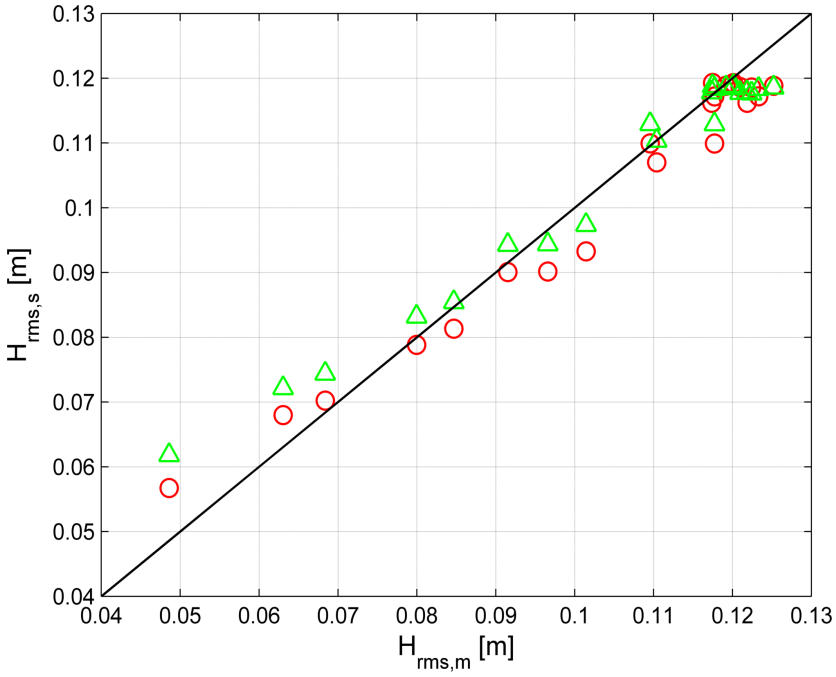

Figure 4-7: SWASH prediction versus measurement of root-mean-square wave height with and without adding bound long waves. With adding bound long waves(red circles) and without adding bound long waves(green triangles).

To distinctly show the differences between the measurement and the cases with or without imposing bound long waves,respectively, the coefficient of determination and root-mean-square error are employed. Figure 4-7 indicates the results of SWASH prediction versus the measurement, the horizontal axis demonstrates the root-mean-square wave height measured in flume and the vertical axis shows the root-mean-square wave height predicted by SWASH at the same position. Note that, the black line represents a state that the computed root-mean-square wave height equals the measured value and hence, the closer to the line the better the result is. Moreover, the coefficient of determination and the root-mean-square error between the predictions and measurement are demonstrated in Table 4-3.

Table 4-3: Coefficient of determination R^2 and root-mean-square error of root-mean-square wave height computed by SWASH with or without adding bound long wave comparing to the measurement

Case	Number of layers	Add bound long waves	R^2	Root-mean-square error
B1	20	Yes	0.9595	0.0044
B2	20	No	0.9530	0.0047

The values of predicted root-mean-square wave height versus measurement are distributed closely to the line $H_{rms,s} = H_{rms,m}$ for both cases in Figure 4-7. The difference between the cases with and without adding bound long waves is relatively small at every fixed point. Table 4-3 indicates that, the simulations show relatively low error and there is no significant difference between these cases, the imposition of bound long waves are not sensitive to the wave height as well as the set-up. Nonetheless, the simulation with adding bound long waves reveals a more accurate and stable result to represent the observation. Subsequently, the sensitivity to the vertical flow structure is studied by means of plotting the mean velocity at 5 cm above the flume bed, which is shown in the following Figure 4-8.

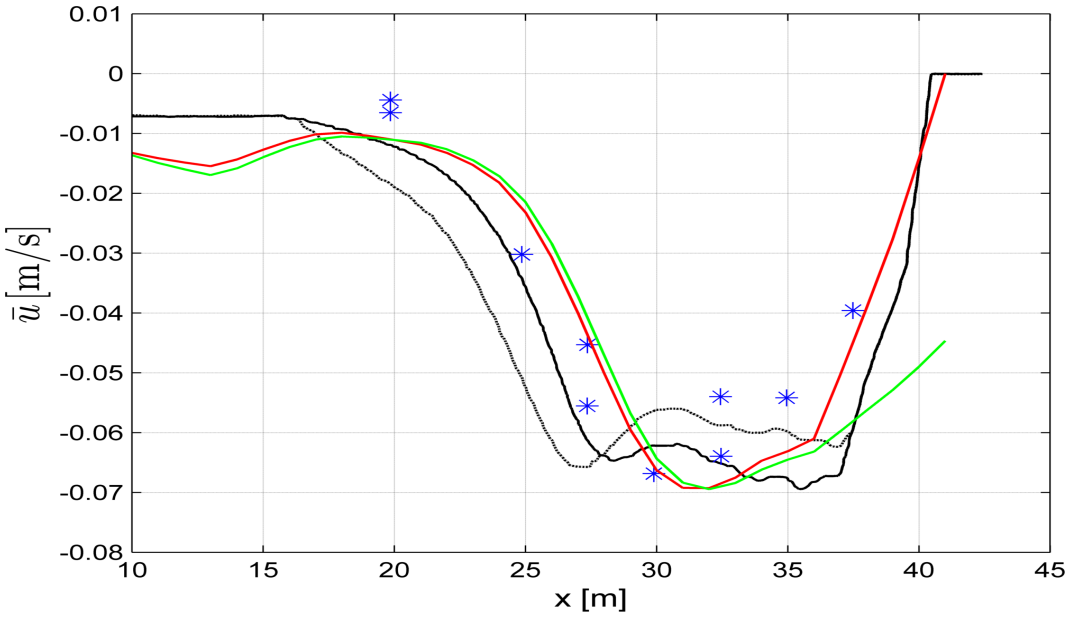

Figure 4-8: Mean velocity at 5 cm above bottom with and without adding bound long waves. Roelvink and Stive with lag(black solid line), Roelvink and Stive without lag(black dashed line), measurements(blue stars), with adding bound long waves(red line) and without adding bound long waves(green line).

In this case, the red and green lines illustrate the predictions of SWASH with and without adding bound long waves, respectively. The vital difference between two cases is found near the shoreline that, the simulation with adding bound long waves shows overall good agreement with the measurement while the case without such an imposition is underestimated near the beach. It may correspond to the overestimation of wave height mentioned above, since the undertow is the offshore directed current compensated for the wave mass flux towards the coast.

Figure 4-9 indicates computed (vertical axis) versus the measured (horizontal axis) mean velocities at 5 cm above the bottom. It is obvious that the red circles represented the case with imposition performs better than the green triangles indicated the case without imposition. In addition, Table 4-4 demonstrates the coefficient of determination and the root-mean-square error between the predicted and measured mean velocities.

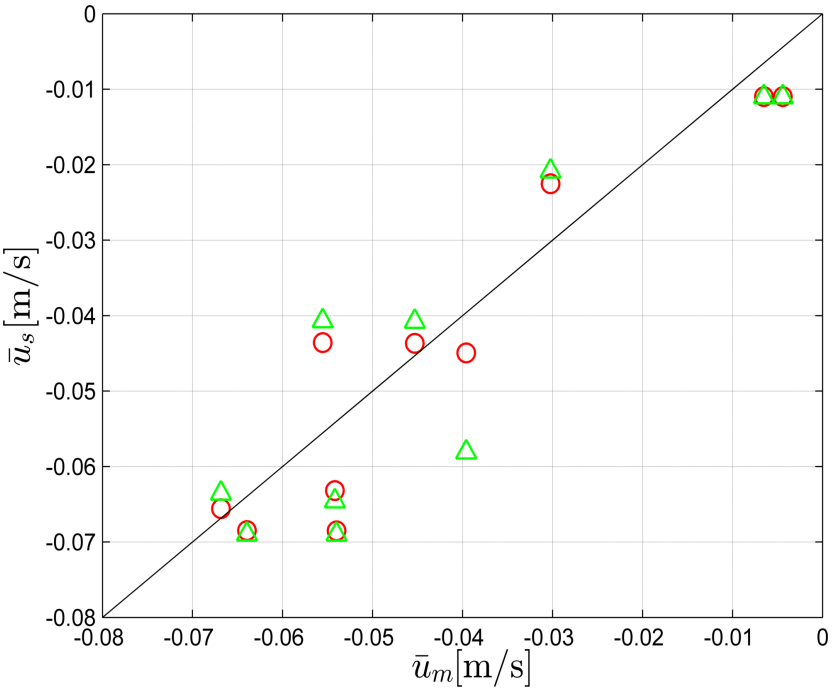

Figure 4-9: SWASH prediction versus measurement of mean velocity at 5 cm above bottom with and without adding bound long waves. With adding bound long waves(red circles) and without adding bound long waves(green triangles).

Table 4-4: Coefficient of determination R^2 and root-mean-square error of mean velocity at 5 cm above bottom computed by SWASH with or without adding bound long waves comparing to the measurement

Case	Number of layers	Add bound long waves	R^2	Root-mean-square error
B3	30	Yes	0.8614	0.0078
B4	30	No	0.7494	0.0105

As can be known from the Table 4-4 that, the vertical velocity is relatively sensitive to the imposition of bound long waves. The simulation with adding bound long waves presents a better fit to the status ($\bar{u}_s = \bar{u}_m$) and a lower error.

In general, the imposition of bound long waves is of utmost importance in predicting water level, wave height, set-up and vertical velocity accurately by SWASH. It may be forecast that, the imposition is essential for the correct approximations of long-wave and asymmetric flows. Consequently, adding the second order bound long waves to the boundary condition would result in more accurate and stable simulation of the cross-shore flows.

4-3-3 Cycle period

Figure 4-5a shows that, even though the simulations performed a relatively good agreement with the observation, deviation still exited especially around the spectral densities of 1 Hz. One of the possibility was that, the wave spectrum imposed in the flume experiment was not an exact JONSWAP spectrum due to the limitation of instrument around that time. As indicated in the model setup that, the wave spectrum can be given in a file, providing a solution to imposing a boundary condition in step with the imposition in the flume test. However, a relatively small frequency interval is not applicable in SWASH yet, only a cycle period of 1000 seconds is adopted in this case. Note that, the cycle period is refer to the time over which the surface elevation and the velocities are synthesized, it should be long enough to obtain reasonably reliable solutions but also short enough to be stationary. Therefore, it is worthwhile to conducted the sensitivity analysis of cycle period.

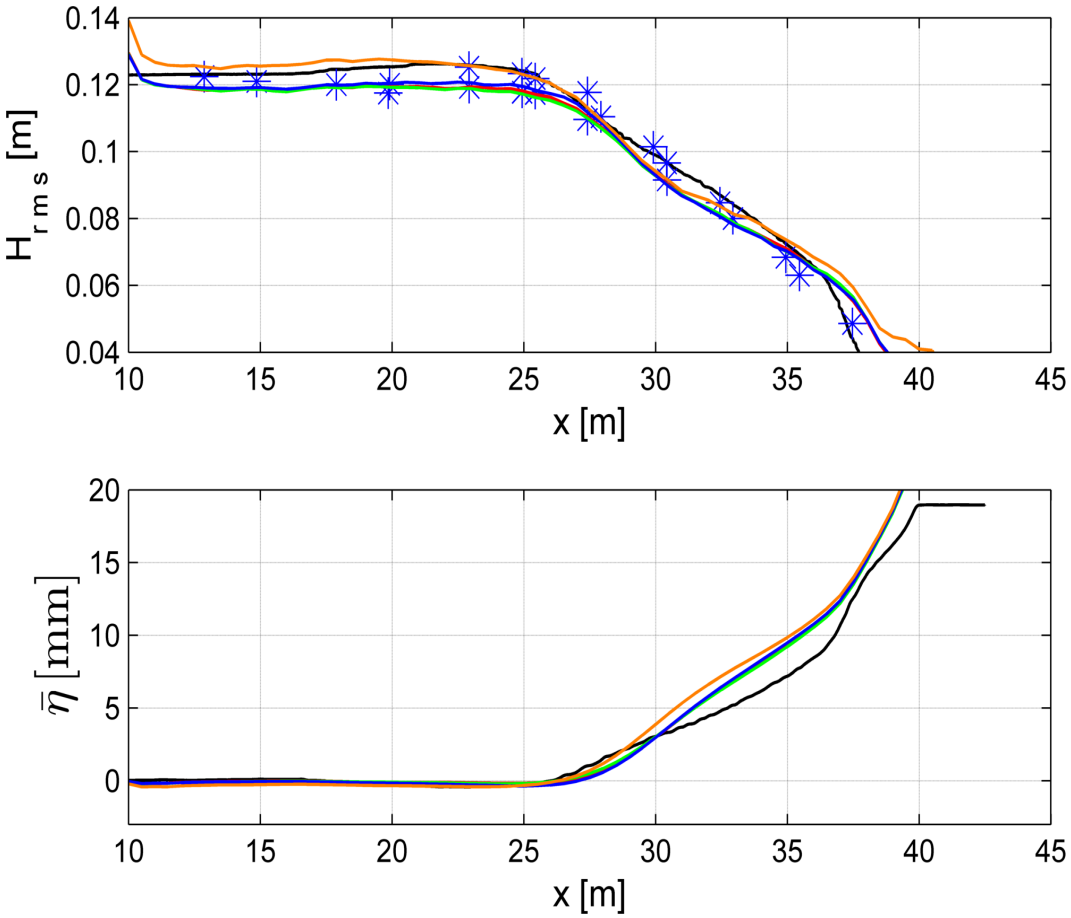

Figure 4-10: Root-mean-square wave height(upper panel) and mean water level set-up(lower panel) along the wave flume with varied cycle period. Roelvink and Stive(black line), measurements(blue stars), cycle period 15 minutes(red line), 30 minutes(green line), 40 minutes(blue line) and boundary condition specified by means of spectrum file with a cycle period of 1000 seconds(orange line).

Figure 4-10 illustrates the results solved by the boundary condition specified by means of spectrum file (SPEC) with cycle period of 1000 seconds and descriptions of spectral parameters with cycle period of 15, 30 and 40 minutes, respectively. It can be observed that, the wave decay prediction of imposing spectrum file is larger than the other cases. As indicated by the Figure 4-11, the relevant root-mean-square wave height is overestimated especially near the offshore boundary. Perhaps the involvement of abundant wave components would lead to unstable computation and hence influence the simulation. Hence, the specification of spectral parameters is employed in this study.

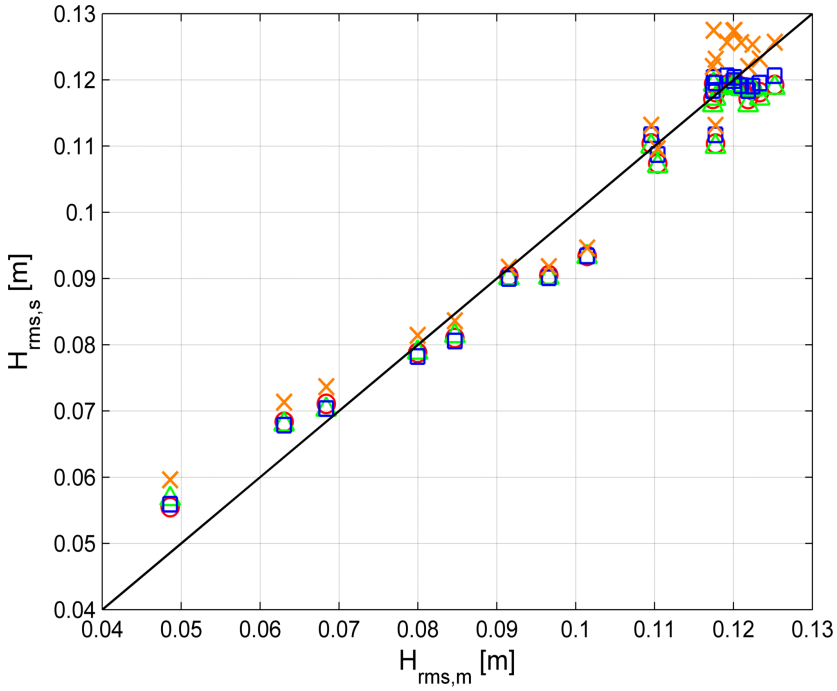

Figure 4-11: SWASH prediction versus measurement of root-mean-square wave height with varied cycle period. Cycle period 15 minutes(red circles), 30 minutes(green triangels), 40 minutes(blue squares) and SPEC 1000 seconds(orange crosses).

Table 4-5: Coefficient of determination R^2 and root-mean-square error of root-mean-square wave height computed by SWASH with varied cycle period comparing to the measurement.

Case	Number of layers	Cycle period	R^2	Root-mean-square error
C1	20	SPEC 1000 seconds	0.9374	0.0055
C2	20	15 minutes	0.9644	0.0041
C3	20	30 minutes	0.959	0.0044
C4	20	40 minutes	0.9685	0.0039

Based on the Table 4-5, case C2, C3 and C4 all present good agreement with the measurement and the differences between each other are relatively small. As a consequence, it may be concluded that the varied cycle period is not sensitive to the predictions of wave height and set-up.

In contrast, the sensitivity of cycle period is more significant to the vertical velocity, which can be found in Figure 4-12. For a cycle period of 30 minutes, the result of mean velocity fit the measurement best while the largest deviation occurred in the case with a cycle period of 40 minutes. It is possible that 40 minutes is too long to get stationary state or the spin-up time is so long (more than 20 minutes) that influence the result.

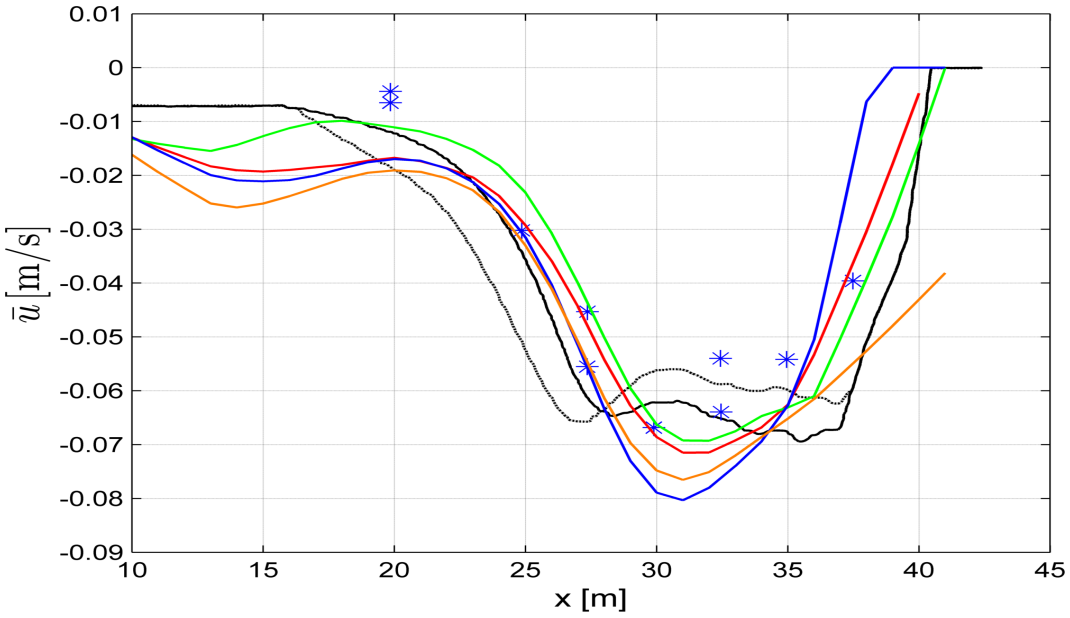

Figure 4-12: Mean velocity at 5 cm above bottom with varied cycle period. Roelvink and Stive with lag(black solid line), Roelvink and Stive without lag(black dashed line), measurements(blue stars), Cycle period 15 minutes(red line), 30 minutes(green line), 40 minutes(blue line) and SPEC 1000 seconds(orange line).

To compare the results with the observation statistically, the values of the prediction versus measurement are plotted in Figure 4-13, in which the black line represents no error. It is obvious that, most of the predicted mean velocities of the case with spectrum file are underestimated as similar with the simulation with a cycle period of 40 minutes. For cycle period of 15 and 30 minutes, the points representing the prediction versus measurement are distributed closer to the black line and hence, the simulating results reach much better agreement with the observation.

The differences are also quantified with the coefficient of determination and root-mean-square error which are indicated in Table 4-6. The optimum was chosen according to the largest coefficient of determination and the smallest root-mean-square error. As a result, a cycle period of 30 minutes was employed in simulation regarding vertical velocity.

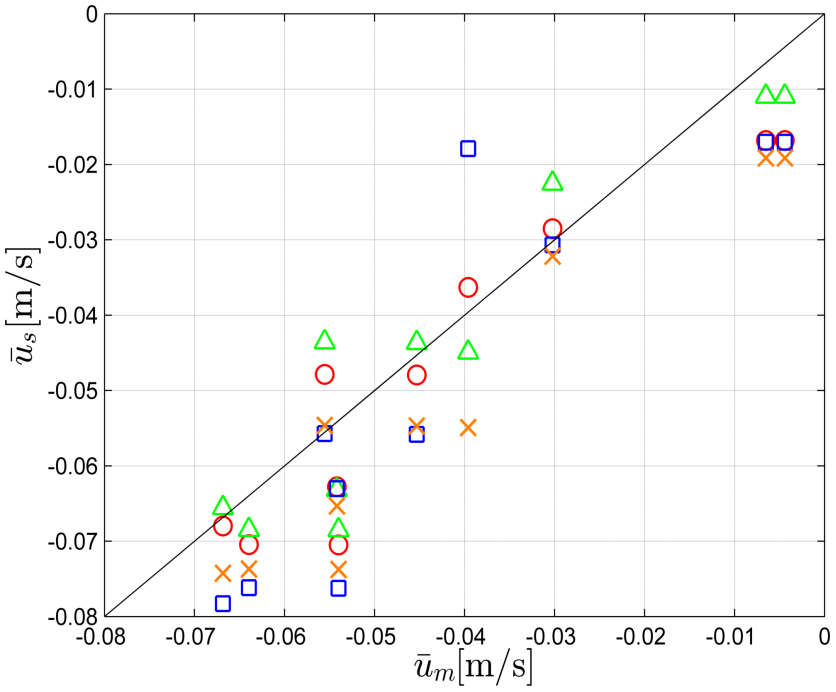

Figure 4-13: SWASH prediction versus measurement of mean velocity at 5 cm above bottom with varied cycle period. Cycle period 15 minutes(red circles), 30 minutes(green triangels), 40 minutes(blue squares) and SPEC 1000 seconds(orange crosses).

Table 4-6: Coefficient of determination R^2 and root-mean-square error of mean velocity at 5 cm above bottom computed by SWASH with varied cycle period comparing to the measurement.

Case	Number of layers	Cycle period[min]	R^2	Root-mean-square error
C5	30	SPEC 1000 seconds	0.6891	0.0117
C6	30	15 minutes	0.8346	0.0085
C7	30	30 minutes	0.8614	0.0078
C8	30	40 minutes	0.6124	0.0131

In conclusion, the wave spectrum can be specified by the measurement given in a file, but the limitation of this imposition might result in significant deviation. Moreover, the cycle period must reach a compromise between long duration to involve sufficient components and short duration to be stationary. Based on the analysis in this subsection, the cases with a cycle period of 30 minutes performed in good agreements with the observations. Consequently, a JONSWAP spectrum specified by spectral parameters was imposed as the boundary condition with a cycle period of 30 minutes in the next chapter.

4-3-4 Bottom Friction

The bottom friction may play a vital role in wave propagation. Also, the involvement of vertical viscosity would transmit the influence of bottom stress to the whole water column. The Nikuradse roughness height was employed since high vertical resolution was considered in all the cases. As indicated before, the Nikuradse roughness height is difficult to estimate accurately and the sensitivity study is hence of essential to determine the correct roughness parameter.

Figure 4-14 presents the predictions with inputting the Nikuradse roughness height of 0.0015 m, 0.003 m and 0.005 m, respectively. It seems that there is no disparity among the results, therefore it is unnecessary to compare the prediction versus observation to the status of perfect agreement. Table 4-7 shows the coefficient of determinations and root-mean-square error for each case and there is no difference in fact. As a result, the bottom friction is not a sensitivity term of wave decay.

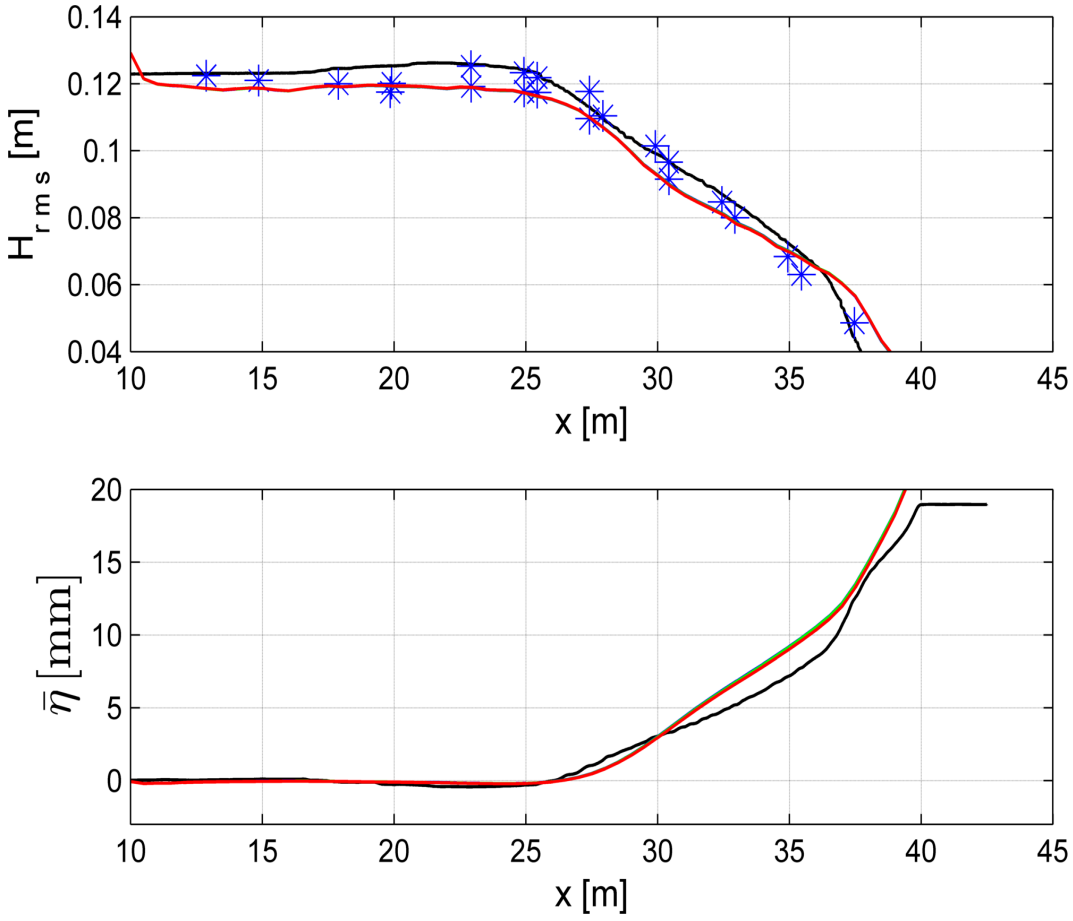

Figure 4-14: Root-mean-square wave height(upper panel) and mean water level set-up(lower panel) along the wave flume with varied roughness. Roelvink and Stive(black line), measurements(blue stars), Nikuradse roughness height 0.0015 m(red line), 0.003 m(green line) and 0.005 m(blue line).

Table 4-7: Coefficient of determination R^2 and root-mean-square error of root-mean-square wave height computed by SWASH with varied roughness comparing to the measurement.

Case	Number of layers	Nikuradse roughness height[m]	R^2	Root-mean-square error
D1	20	0.0015	0.959	0.0044
D2	20	0.003	0.959	0.0044
D3	20	0.005	0.9595	0.0044

The bottom roughness may impact the vertical flow structure since it would be extended to the entire water column by the vertical viscosity. The predictions of mean velocity above 5 cm above the bottom are illustrated in Figure 4-15. However, the differences between each other case were still small, the vertical velocity showed a relatively low sensitivity to the bottom roughness as well. Figure 4-16 indicates that the distributions of predictions versus measurement were almost the same but the case with a Nikuradse roughness height of 0.0015 m shows some deviation.

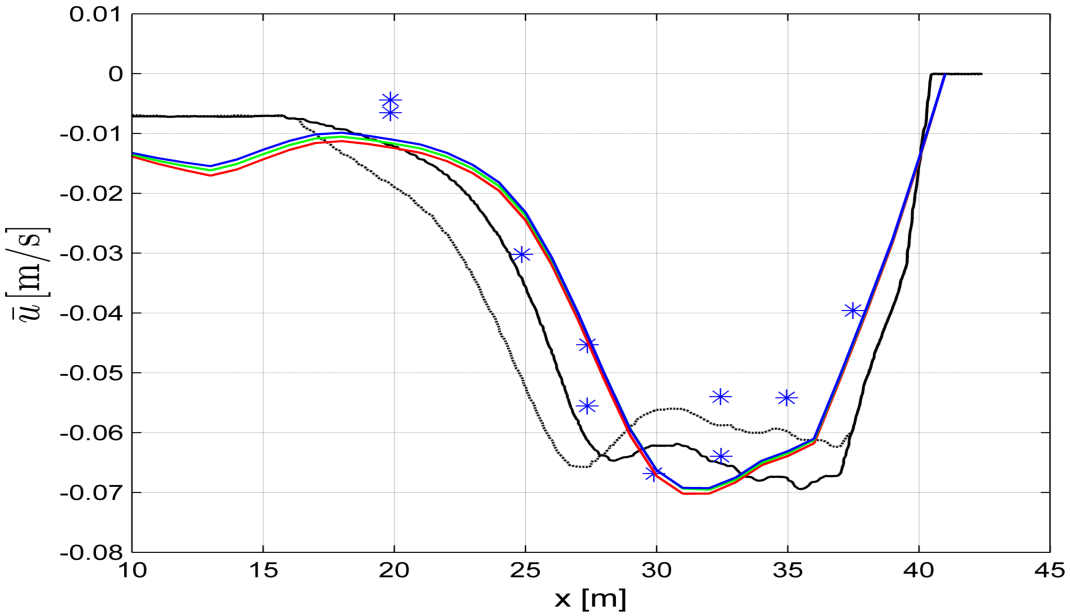

Figure 4-15: Mean velocity at 5 cm above bottom with and without adding bound long waves with varied roughness. Roelvink and Stive with lag(black solid line), Roelvink and Stive without lag(black dashed line), measurements(blue stars), Nikuradse roughness height 0.0015 m(red line), 0.003 m(green line) and 0.005 m(blue line).

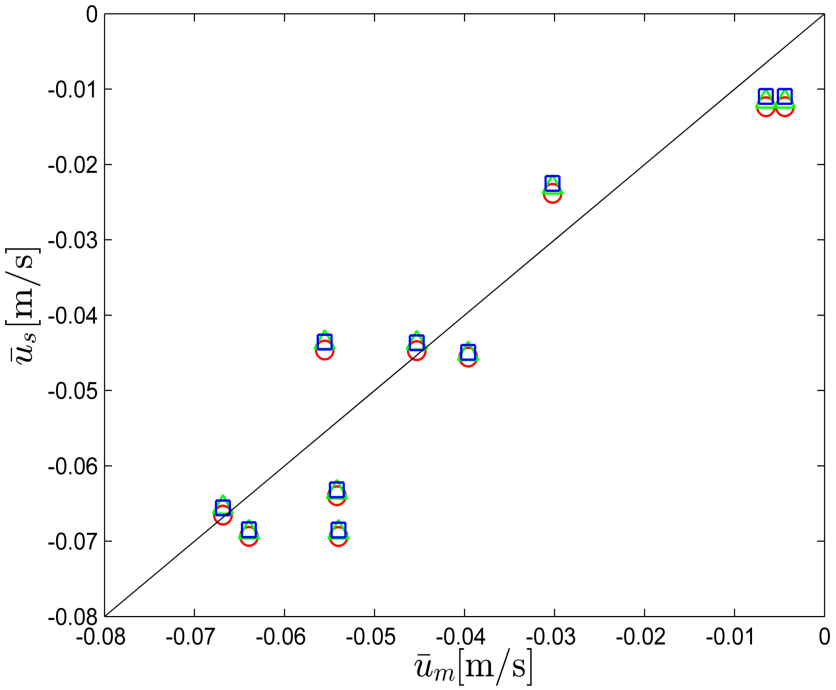

Figure 4-16: SWASH prediction versus measurement of mean velocity at 5 cm above bottom with varied roughness. Nikuradse roughness height 0.0015 m(red circles), 0.003 m(green triangles) and 0.005 m(blue squares).

Table 4-8: Coefficient of determination R^2 and root-mean-square error of mean velocity at 5 cm above bottom computed by SWASH with varied roughness comparing to the measurement.

Case	Number of layers	Nikuradse roughness height[m]	R^2	Root-mean-square error
D4	30	0.0015	0.8513	0.0081
D5	30	0.003	0.8555	0.0080
D6	30	0.005	0.8614	0.0078

As can be seen in the Table 4-8, the coefficient of determinations and root-mean-square errors were calculated to choose the optimal Nikuradse roughness height. It is obvious that the simulation with a Nikuradse roughness height of 0.005 m performed in the best agreement, with the largest coefficient of determination and also the lowest error.

To conclude, the bottom friction is not a dominant contribution to the predictions of the wave decay as well as the vertical velocity. In this study, the Nikuradse roughness height was set as 0.005 m, because it provided the highest degree of closeness to the observation. Even though the differences were relatively small.

4-3-5 Discretization of Advection Terms

As shown in the Table 3-1, there are 8 sets of numerical schemes for the discretization of the advection terms in the governing momentum equations. These schemes are recommended to simulate the vertical flow structure accurately. In fact, all the combinations were adopted in sensitivity analysis to find the optimal settings. However, when using the central difference scheme to discretize the horizontal advection term of u momentum equation, SWASH became unstable. As a result, the central difference scheme was not applied for discretizing the horizontal advection term $\frac{\partial uu}{\partial x}$. The following Table 4-9 summarized the combinations of schemes using in discretizing the advection terms.

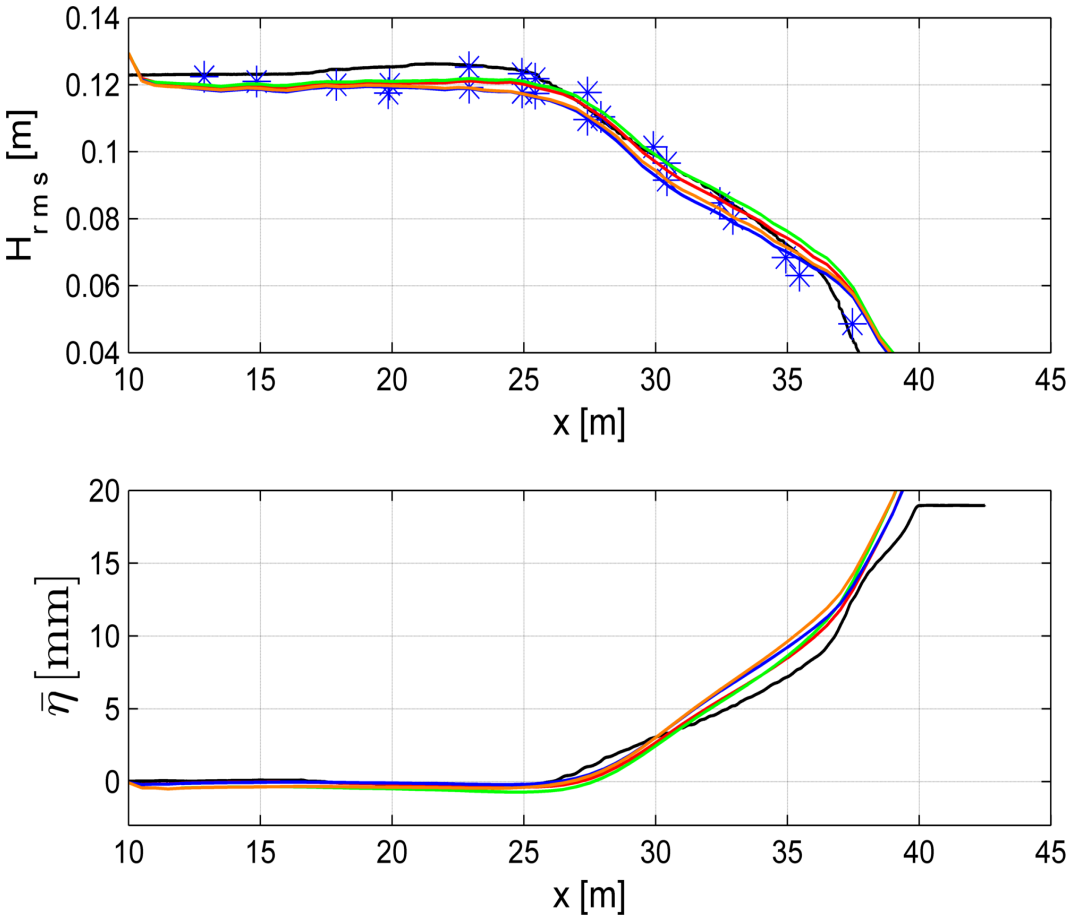

Figure 4-17: Root-mean-square wave height(upper panel) and mean water level set-up(lower panel) along the wave flume with different combination of schemes employed for discretizing advection terms. Roelvink and Stive (black line), measurements(blue stars), set of schemes(summarized in Table 4-9) S1(red line), S2(green line), S3(blue line) and S4(orange line).

The simulated wave height and set-up of which the advection terms were approximated by different schemes are presented in Figure 4-17. The difference between the predictions of S1 and S2 is relatively small and the results of S3 and S4 almost cover each other. Hence the wave decay is not sensitive to the discretization of horizontal advection term $\frac{\partial uw}{\partial x}$. For the prediction of root-mean-square wave height, the approximations of S1 and S2 are slightly

Table 4-9: Model set-up for sensitivity study of discretization of advection terms (BDF: Backward Differentiation Formula scheme; CDS: Central Differences Scheme; UPW: first order UPWIND scheme)

Set	Horizontal advetion $\frac{\partial uu}{\partial x}$	Horizontal advetion $\frac{\partial uw}{\partial x}$	Vertical advetion $\frac{\partial wu}{\partial z}$	Vertical advetion $\frac{\partial ww}{\partial z}$
S1	BDF	BDF	UPW	UPW
S2	BDF	CDS	UPW	UPW
S3	BDF	BDF	CDS	UPW
S4	BDF	CDS	CDS	UPW

larger than the predictions of S3 and S4, while the set-up presents the other way around. By comparing with the horizontal advection term, sensitivity of wave decay is more significant with changing the scheme for the vertical advetion term $\frac{\partial wu}{\partial z}$.

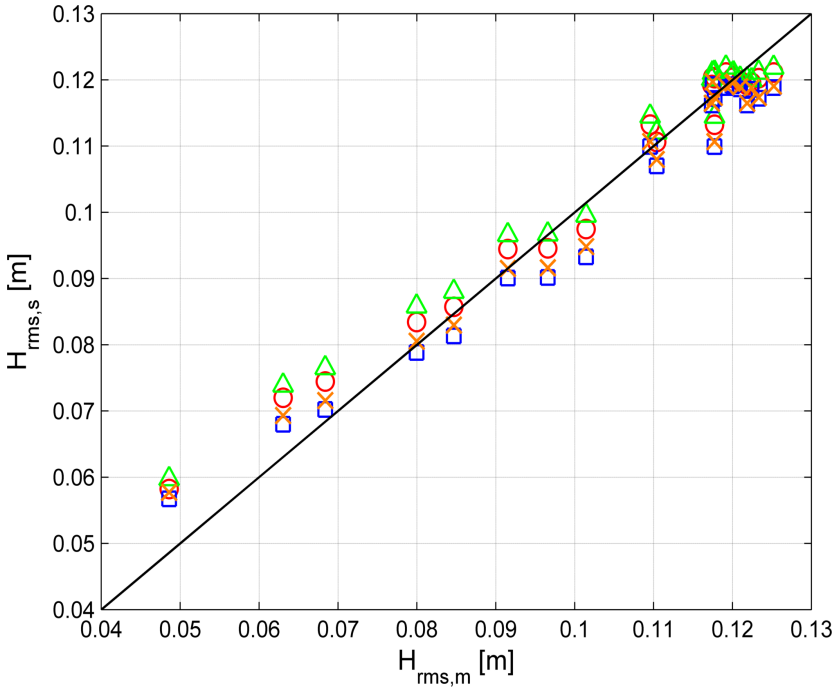

Figure 4-18: SWASH prediction versus measurement of root-mean-square wave height with different combination of schemes employed for discretizing advection terms. S1(red circles), S2(green triangles), S3(blue squares) and S4(orange crosses).

Figure 4-18 shows how the predictions of root-mean-square wave height fit the observation. The result of S1 was fairly close to the black line which represent the prediction equals measurement. The result of S2 was mostly overestimated while the calculations of S3 and S4 were underestimated at most of the locations. Moreover, Table 4-10 also indicates that, the case of S1 was the best performance for wave decay.

Table 4-10: Coefficient of determination R^2 and root-mean-square error of root-mean-square wave height computed by SWASH with different combination of schemes employed for discretizing advection terms comparing to the measurement.

Case	Number of layers	Set of schemes	R^2	Root-mean-square error
E1	20	S1	0.9667	0.004
E2	20	S2	0.9539	0.0047
E3	20	S3	0.9595	0.0044
E4	20	S4	0.9631	0.0042

Emphasizing again, in this study the prediction of undertow was represented by the mean velocity at 5 cm above the bottom level. The relevant differences between each case can be seen in the Figure 4-19. There was little difference between the results of S1 and S2 as well as of S3 and S4. Thus, it seems that the return current is not sensitive to varied schemes to approximate the horizontal advection term $\frac{\partial uw}{\partial x}$. In addition, the predicted mean velocities, with different schemes for approximating the vertical advetion term $\frac{\partial wu}{\partial z}$(e.g. S1 versus S3), show relatively large difference in the surf zone(approximately x $>$ 27 m) but converge near the shoreline. Based on the Figure 4-18, the breaking point might be around x=25 m. It is possible that the difference could be relative to the wave breaking.

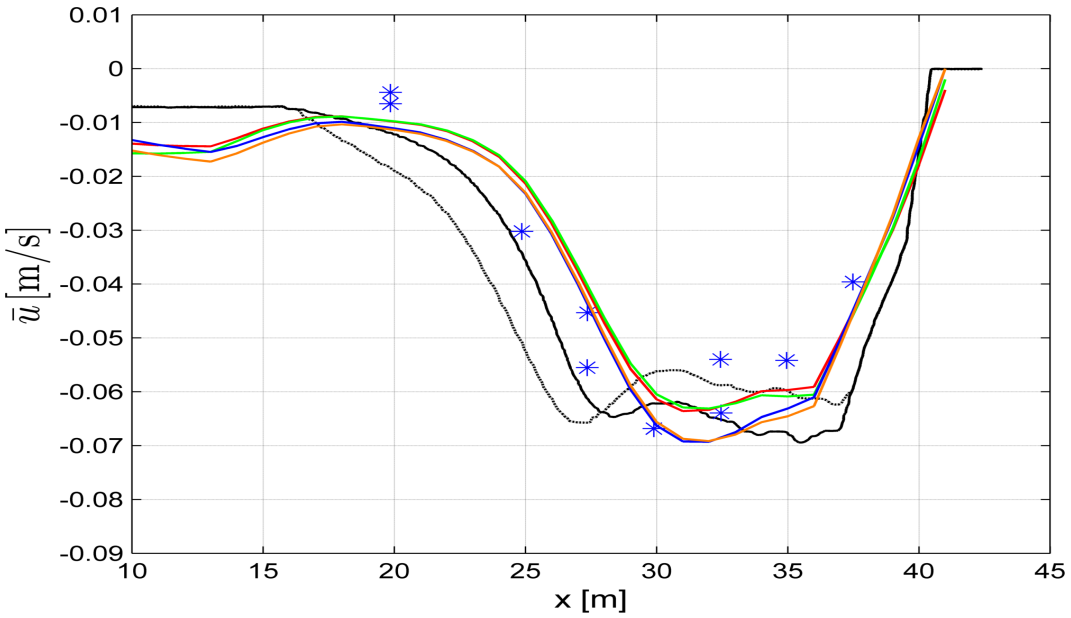

Figure 4-19: Mean velocity at 5 cm above bottom with different combination of schemes employed for discretizing advection terms. Roelvink and Stive with lag(black solid line), Roelvink and Stive without lag(black dashed line), measurements(blue stars), set of schemes S1(red line), S2(green line), S3(blue line) and S4(orange line).

The distributions of predicted versus measured mean velocities at 5 cm above the bottom are illustrated in Figure 4-20. It can be discovered that, SWASH predictions of S1 and S2 were close to the measurement. In contrast, results of S3 and S4 were relatively underestimated at most observation locations. Moreover, the breaking-induced roller is not incorporate in

SWASH. It was expected that the result of undertow would be overestimated, which will be explained later. Hence, the vertical advetion term in simulating return current would be approximated by the first order upwind scheme(UPW). Based on Table 4-11 that, S1 showed the highest coefficient of determination and lowest root-mean-square error and hence adopted in the simulations of wave decay and vertical flow structure.

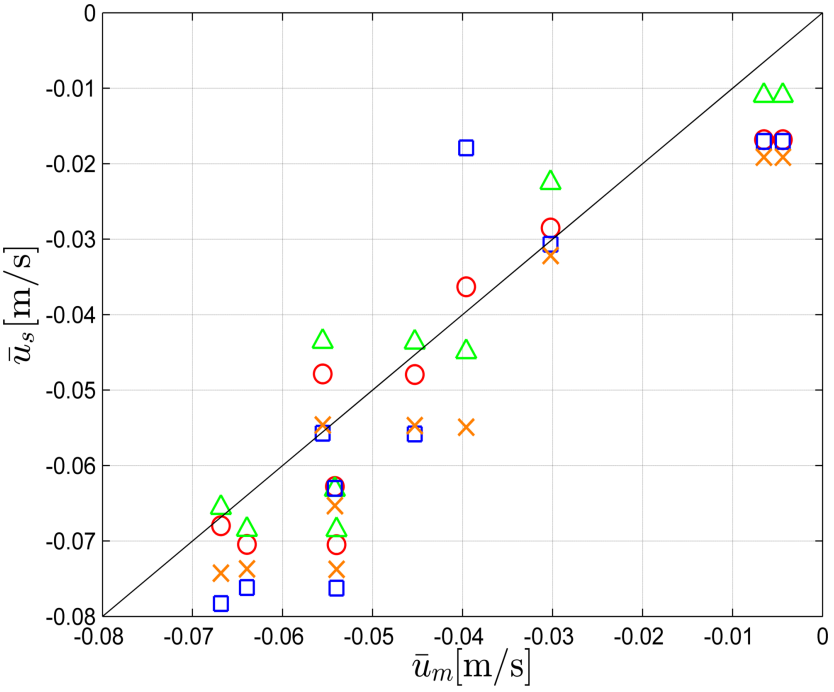

Figure 4-20: SWASH prediction versus measurement of mean velocity at 5 cm above bottom with different combination of schemes employed for discretizing advection terms. S1(red circles), S2(green triangles), S3(blue squares) and S4(orange crosses).

Table 4-11: Coefficient of determination R^2 and root-mean-square error of mean velocity at 5 cm above bottom computed by SWASH with different combination of schemes employed for discretizing advection terms comparing to the measurement.

Case	Number of layers	Set of schemes	R^2	Root-mean-square error
E5	30	S1	0.8788	0.0073
E6	30	S2	0.8623	0.0078
E7	30	S3	0.8614	0.0078
E8	30	S4	0.8464	0.0082

In summary, both the wave decay and mean velocity were not sensitive to varied schemes for discretizing the horizontal advection term $\frac{\partial uw}{\partial x}$, but they could be influenced by different schemes for the discretization of vertical advetion term $\frac{\partial wu}{\partial z}$. In this study, the horizontal advection terms employed the backward difference scheme (BDF) while the vertical advetion terms were approximated by means of first order upwind scheme.

4-3-6 Discretization of Water Depth in Velocity Points

The staggered grid is implemented in SWASH and thus, the water depth and velocity points are defined at alternate grid points. However, the usual interpolation may result in relatively large error, an appropriate solution is adopting upwind scheme for discretizing the water depth in velocity points. The following paragraphs present the sensitivities of wave decay and mean velocity, respectively, to varied schemes of discretization, namely first order upwind scheme, central difference scheme and a second order interpolation augmented with MUSCL flux limiter.

In the simulation of wave decay, changing schemes of discretization for water depth in velocity points would influence the wave height as well as the water set-up, see Figure 4-21. For the prediction of root-mean-square wave height, the water depth approximated by first order upwind scheme is more deviated while employing the default MUSCL flux limiter leads to overestimation of water set-up. A special attention is given to the central difference scheme, since it shows relatively accurate predictions for both wave height and set-up.

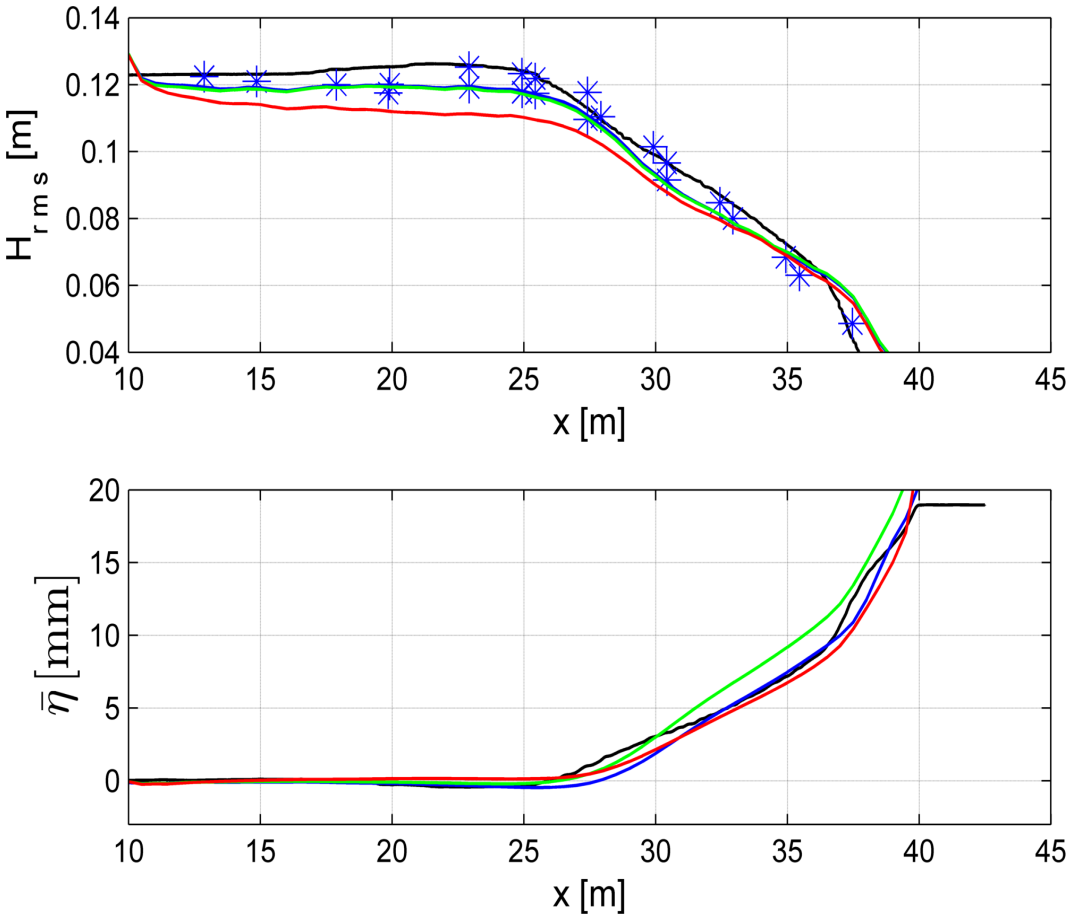

Figure 4-21: Root-mean-square wave height(upper panel) and mean water level set-up(lower panel) along the wave flume with different discretization for water depth at velocity points. Roelvink and Stive(black line), measurements(blue stars), First order upwind(red line), default MUSCL(green line) and central difference(blue line).

As can be seen in Figure 4-22 that, the computed root-mean-square wave height was evidently underestimated in the case of first order upwind scheme while the other cases fitted relatively well to the line of perfect agreement. Moreover, Table 4-12 indicates the central difference scheme gave the best reproduction of root-mean-square wave height with the largest coefficient of determination and the lowest error. In overall, the central difference scheme is recommended in modelling wave decay.

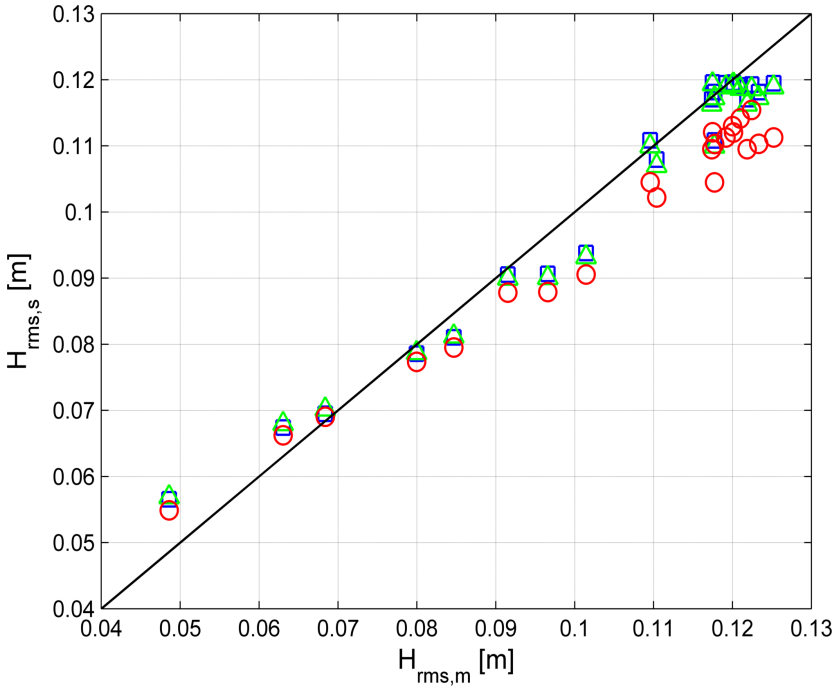

Figure 4-22: SWASH prediction versus measurement of root-mean-square wave height with different discretization for water depth at velocity points. First order upwind(red circles), MUSCL(green triangles) and central difference(blue squares).

Table 4-12: Coefficient of determination R^2 and root-mean-square error of root-mean-square wave height computed by SWASH with different discretization for water depth at velocity points comparing to the measurement.

Case	Number of layers	Scheme	R^2	Root-mean-square error
F1	20	UPW	0.8576	0.0082
F2	20	MUSCL	0.9595	0.0044
F3	20	CDS	0.9666	0.0040

The predictions of mean velocity at 5 cm above bed level are compared in Figure 4-23, the sensitivity of mean velocity is fairly significant to different schemes of discretization for water depth in velocity points. The case of applying first order upwind scheme gave the best prediction. However, the second order interpolation augmented with MUSCL flux limiter was expected to be more appropriate in the beginning. In fact, the prediction with MUSCL limiter was in fairly good agreement before the breaking point but deviated too much after that. The reason is still unclear yet, perhaps the application of MUSCL limiter and central difference scheme would generate increasing wiggles and SWASH become unstable as a consequence.

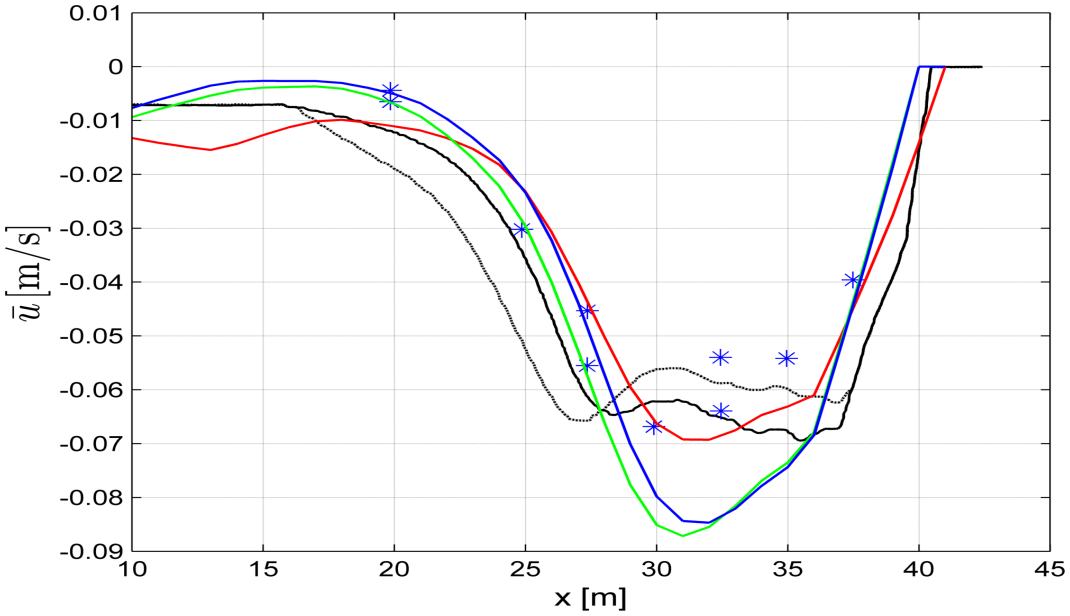

Figure 4-23: Mean velocity at 5 cm above bottom with and without adding bound long waves with different discretization for water depth at velocity points. Roelvink and Stive with lag(black solid line), Roelvink and Stive without lag(black dashed line), measurements(blue stars), First order upwind(red line), default MUSCL(green line) and central difference(blue line).

Furthermore, the predictions versus observations of mean velocity are plotted in Figure 4-24. Most of the mean velocities were underestimated for each case, especially for the simulations applying MUSCL limiter and central difference scheme, respectively. Additionally, based on Table 4-13, the predicted mean velocity of first order scheme shows a relatively good agreement to the measurement comparing to the other cases. Therefore, the first order upwind scheme was chosen to approximate the water depth in velocity points to achieve an accurate simulation of vertical flow structure.

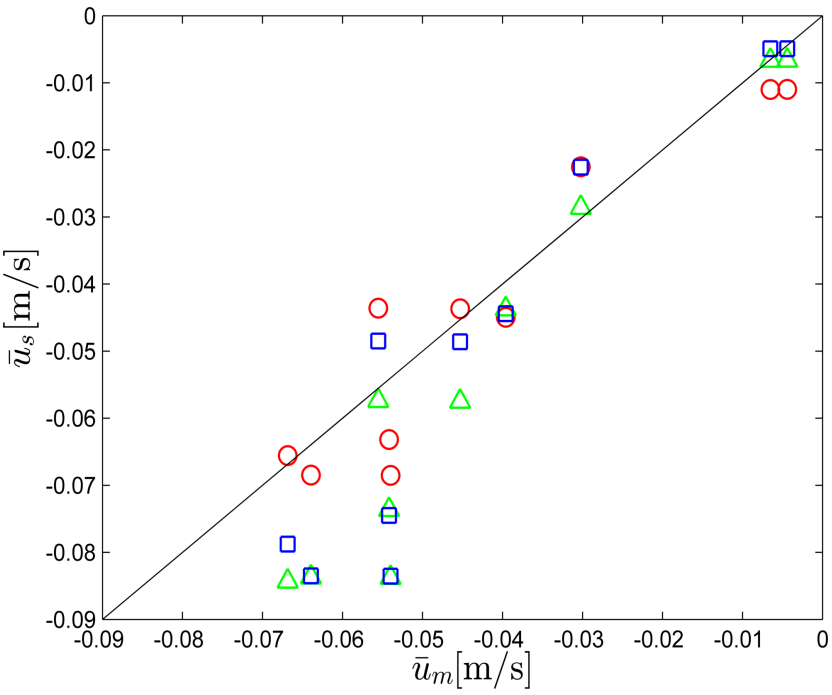

Figure 4-24: SWASH prediction versus measurement of mean velocity at 5 cm above bottom with different discretization for water depth at velocity points. First order upwind(red circles), MUSCL(green triangles) and central difference(blue squares).

Table 4-13: Coefficient of determination R^2 and root-mean-square error of mean velocity at 5 cm above bottom computed by SWASH with different discretization for water depth at velocity points comparing to the measurement.

Case	Number of layers	Scheme	R^2	Root-mean-square error
F4	30	UPW	0.8614	0.0078
F5	30	MUSCL	0.5142	0.0146
F6	30	CDS	0.5556	0.0140

In conclusion, the wave decay as well as the vertical mean velocity showed fairly large sensitivity to varied schemes for discretizing the water depth in velocity points. When simulating the wave decay, the central difference scheme provided better prediction than the other schemes. But differently, for the simulation of undertow, the first order upwind scheme was recommended for approximating the water depth in velocity points. In addition, a further research is recommended to investigate the stability of the second order accurate schemes for discretizing water depth in velocity points, namely the MUSCL limiter and central difference scheme, etc.

Chapter 5

Result

In this chapter, SWASH was used to reproduce a wave flume experiment carried out by Roelvink and Stive[21] with the optimal settings mentioned in last chapter. The results are discussed with regard to wave spectrum, wave height, water set-up and undertow, respectively. The predictions are compared to the measurement in Section 5-1, to investigate the possibility of SWASH for modelling these coastal phenomena accurately. In the next stage, Fast Fourier Transform(FFT) was applied to decompose the time-varying flow velocity calculated by SWASH in Section 5-2, to components with low and high frequency, respectively. In Section 5-3, the central odd flow moments which represent the effects of long wave and asymmetric oscillatory flows, can be computed.

5-1 Result of SWASH

In the following, the numerical solutions of SWASH are discussed to assess whether it is capable of simulating the coastal phenomena related to cross-shore flows. The required predictions are surface density spectrum, wave height, set-up, mean and total velocity. The model results are compared to the observations of flume experiment mentioned in Section 4-1.

5-1-1 Surface elevation spectrum

The surface elevation density spectra at three locations are shown in Figure 5-1 in the dimensionless form. The chosen locations represent the wave-maker boundary(x=10 m), surf zone (x=30.7 m) and more shoreward area (x=32.5 m), respectively. These spectra were obtained by means of Fourier transform with smoothing.

The SWASH predicted spectra agreed well with the measurements at all the locations especially the prediction of high frequency waves. Moreover, the energy of low frequency waves increased in the shoreward direction. This is due to the generation of wave grouping-induced long waves. In addition, the overestimation of energy in low frequencies shown in Figure 5-1a is due to the imposition of second order bound long waves at the boundary.

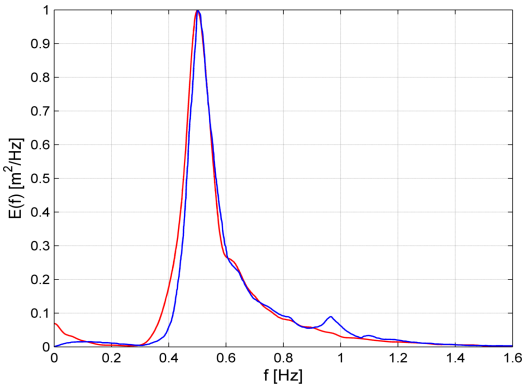

(a) Surface density spectrum at x=10m

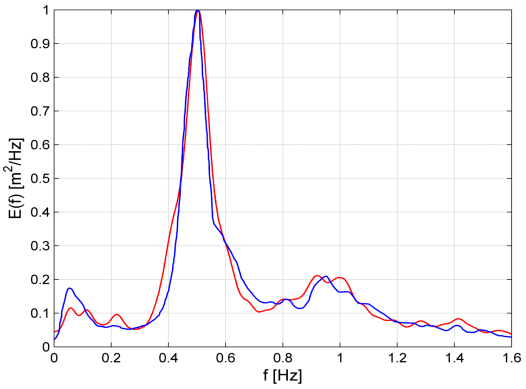

(b) Surface density spectrum at x=30.7m

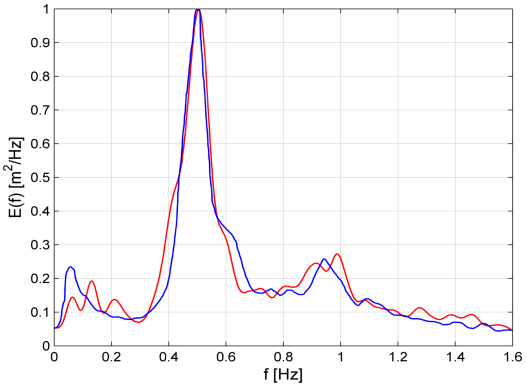

(c) Surface density spectrum at x=32.5m

Figure 5-1: Dimensionless smoothed surface density spectrum at wave maker boundary(x=10m) and in the surf zone(x=30.7m and x=32.5m). Measurements(blue line), SWASH predictions(red line).

As can be seen in Figure 5-1b and Figure 5-1c that, the spectral densities in low frequencies(frequency smaller than 0.25 Hz) present relatively large deviation comparing to the components of high frequency. One possible influencing factor is the imposed boundary condition, since an exact JONSWAP spectrum was not easy to be generated in the laboratory 25 years ago. Even though the wave spectrum can be given in a file, it was not applicable in this study based on the sensitivity study. The limitation is that, a relatively small frequency interval is not applicable in SWASH yet, which might result in significant deviation. Therefore, the imposition of wave spectrum given in a file is desired to be developed.

5-1-2 Wave decay

The undertow is defined as a compensation for the balance between the horizontal gradient of the radiation stress and the wave set-up-induced pressure gradient. Thus, it is essential to study on the wave height and set-up before calculating the return current.

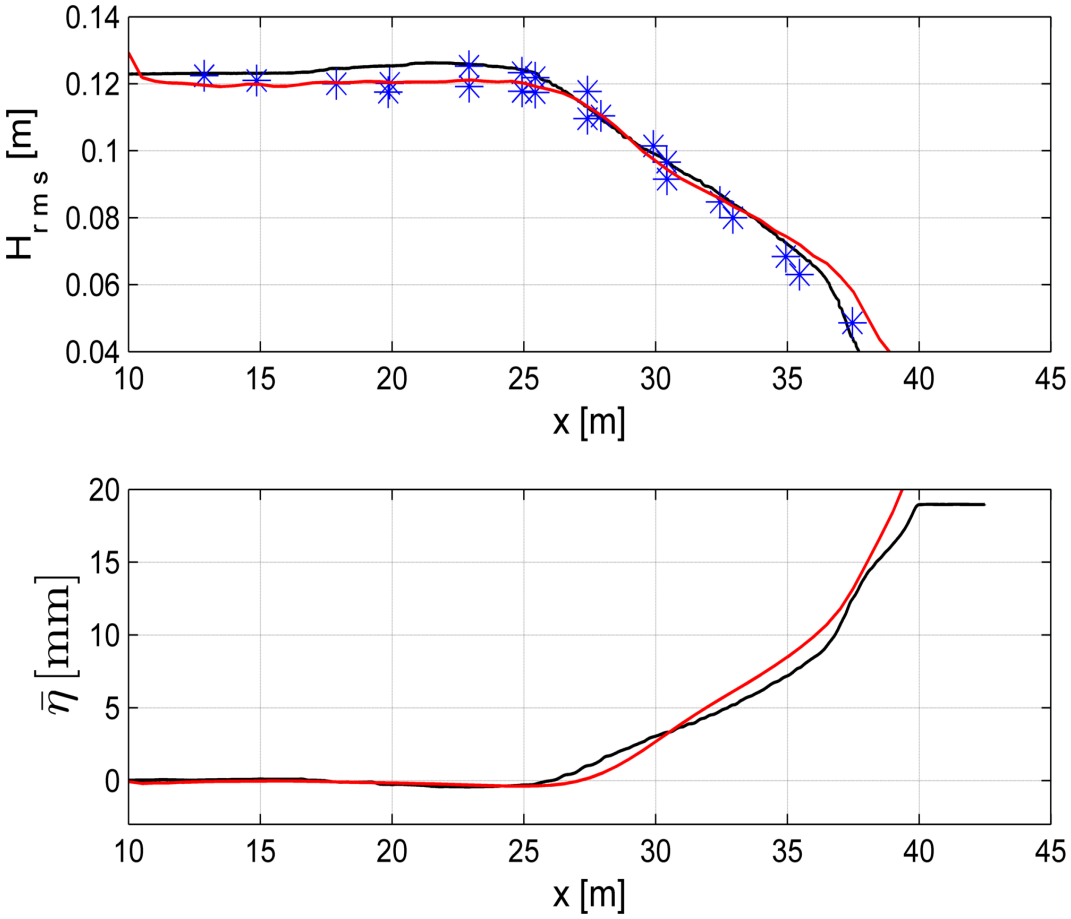

Figure 5-2: Root-mean-square wave height(upper panel) and mean water level set-up(lower panel) along the wave flume. Roelvink and Stive (black line), measurements(blue stars), SWASH predition(red line).

SWASH gave overall good predictions of root-mean-square wave height and set-up comparing to the observations, see Figure 5-2. Not only the magnitude of wave decay but also the location of short wave breaking were shown in relatively good agreement. Particularly, the wave height at the wave-maker boundary was overestimated. It may be explained by the re-reflection even though a weakly reflective boundary condition was imposed. Moreover, SWASH overestimated the wave height in the very shallow. It may be associated with the horizontal turbulent mixing which might influence the wave height near the shoreline found by Rijnsdorp [18]. However, to avoid complicated problems only vertical turbulent mixing was considered in this study. In general, SWASH is capable of accurately simulating the wave decay, including the wave height, set-up and breaking point.

5-1-3 Undertow

A special attention should be given to the simulation of undertow since it is one of the cross-shore flows that contributes to the velocity moments. The undertow is the offshore directed current that compensate the shoreward wave mass flux. The roller might play an important role in predicting the vertical flow structure, since it might dissipate gradually and generate turbulence in the water column beneath. The relation can be expressed by the following equation [25]:

$$\int_{z_b}^{z_b+d} \bar{u} dz = -\frac{M_s + M_r}{\rho} \tag{5-1}$$

in which, z_b represents the bottom level, d is the water depth, $\bar{u}$ indicates the flow rate of undertow, M_s and M_r are the Stokes mass flux and roller mass flux, respectively.

Nevertheless, the study of undertow was represented by the mean velocity at 5 cm above the bottom level rather than the mean velocity under wave trough. It was probably due to the limitation of the measuring instrument decades ago. In Figure 5-3, the comparisons among measurement, SWASH prediction, calculations based on model of Roelvink and Stive(1989) [21] with and without lag were indicated with respect to mean velocity at 5 cm above the bed level.

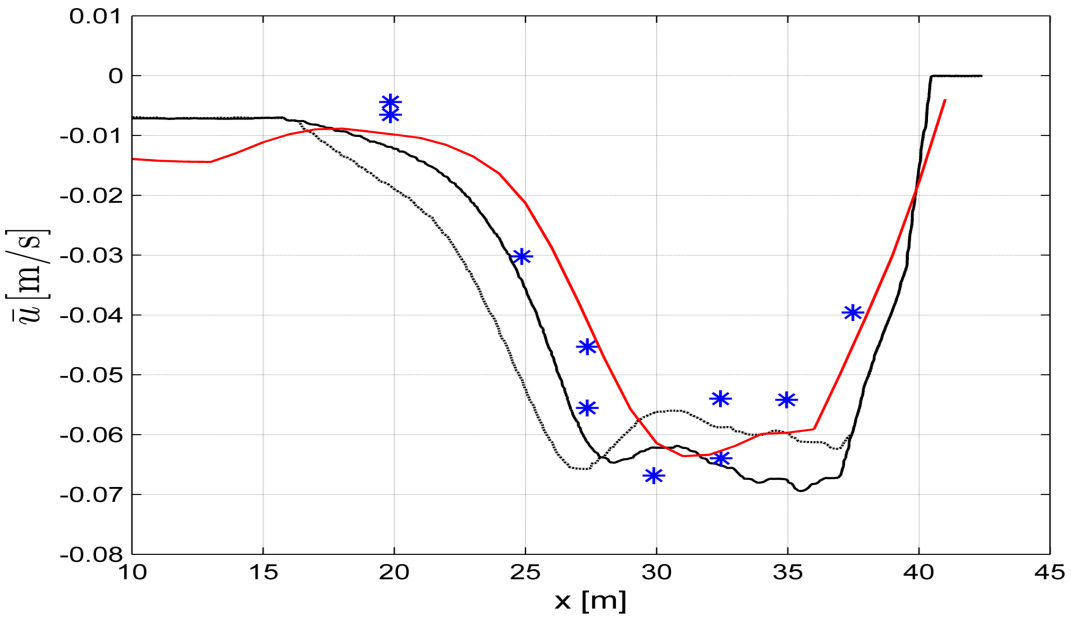

Figure 5-3: Mean velocity at 5 cm above bottom. Roelvink and Stive with lag(black solid line), Roelvink and Stive without lag(black dashed line), measurements(blue stars), SWASH prediction(red line).

As can be seen in Figure 5-3, the SWASH predicted mean velocity demonstrates overall good agreement with the observation. Up to x=30 m, the mean velocity was overestimated. In contrast, SWASH underestimates the mean velocity near the beach (x>30 m). This may be corresponded to an overestimated lag between dissipation and production of the turbulent kinetic energy. The further reason could be the absence of the turbulent production due to roller in SWASH. The breaking-induced turbulence is probably of great importance to the undertow. As a result, the contribution of surface roller should be implemented in the SWASH.

However, the mean velocity at 5 cm above the bottom cannot represent the undertow exactly. It is more recommended to illustrate the vertical flow structure in the entire water column. Therefore, a new experiment of measuring vertical velocities along the water column is expected in the future research.

In addition, the total velocity was obtained as the same settings of mean velocity. The predicted signal of total velocity are decomposed into low and high frequency components, respectively. Finally, the central odd moment flows are computed to analyse how these cross-shore flows contribute to the velocity moments.

5-2 Result of Decomposition

The outputted velocity is a record as a function of time. The fast Fourier transform was applied to distinct different wave components in terms of frequency. As illustrated in Figure 5-4, the horizontal axis presents the time while the vertical axis indicates the amplitude of velocity in blue line. This is the signal of total velocity at 5 cm above the bed level in approximately x=20 m. The red line demonstrates the signal of low wave frequency(f<0.25 Hz), which was obtained by means of fast Fourier transform. Since the measuring location of velocity was set at 5 cm above the bottom, an interpolation was required. A special attention should be given to that, the Fourier transform and filtering process must be done before the interpolation. Otherwise, immeasurable information of wave signal might vanish after interpolating and the result might be incorrect.

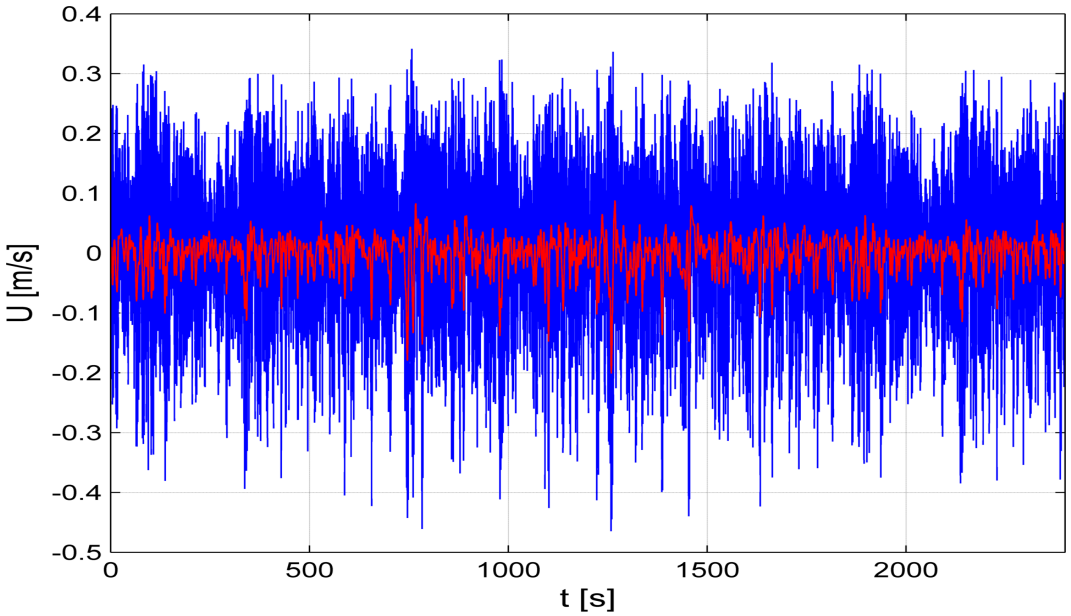

Figure 5-4: Extracted signals of low frequency range(<0.25 Hz)from the total velocity at 5 cm above bottom. Total velocity(blue line) and low frequency flow component(red line).

To investigate the behaviour of wave grouping-induced long wave flow, the extracted signals of low frequencies were raised to the power of 2 and the computed values were averaged over time to get $< {U_L}^2 >$. The averaged flow variances are presented in Figure 5-5, with horizontal axis indicating the distance from the wave generator(left to right) and vertical axis representing the flow variance $< {U_L}^2 >$. Additionally, the blue stars are the observations, the black diamonds present the calculation based on bound long wave theory [21] and the red circles indicate the results computed in this thesis, by filtering the low frequency components from the SWASH predictions.

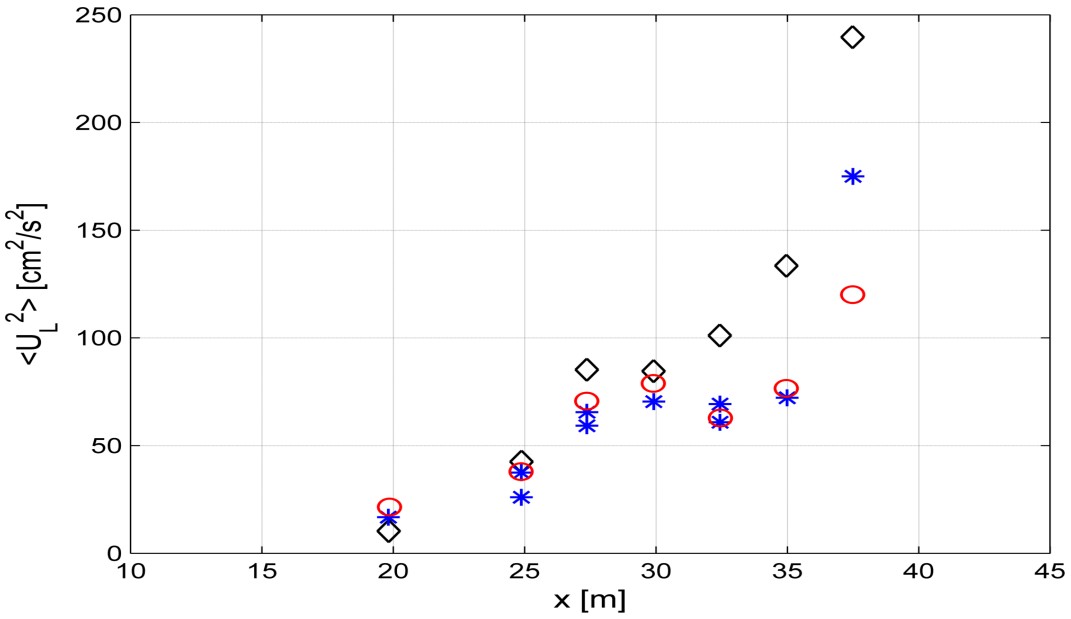

Figure 5-5: Variance of wave grouping-induced long-wave flow $< {U_L}^2 >$. Measurements(blue stars), predictions based on bound long wave theory(black diamonds) and predictions according to SWASH and decomposition(red circles).

The predicted absolute values of long wave variance $< {U_L}^2 >$ are in fairly good agreement to the measurements in general. The only exception occurred at the nearest observation point to the shoreline. It could be acceptable since the location is relatively shallow and the turbulent mixing here is too complicated to analyse. In conclusion, SWASH is capable of simulating the wave grouping-induced long wave flow satisfactorily. Its contribution to the cross-shore velocity moments are discussed and compared to the other components in the next section.

5-3 Cross-shore flows

The undertow and long wave flow variance have been obtained above and the asymmetric oscillation flow can be computed as same as the long wave flow. In this case, the contributions to the odd moment proportional to the bed load transport in cross-shore direction would be investigated and compared with each other. Recall the equation used to evaluate the contributions:

$$< U|U|^2 >= 3 < \bar{U}|U_S|^2 > + < U_S|U_S|^2 > +3 < U_L|U_S|^2 > \tag{5-2}$$

in which, $< \bar{U}|U_S|^2 >$ represents the contribution to the odd moment of the mean flow velocity. The following term $< U_S|U_S|^2 >$ is the central, odd flow moment due to the wave asymmetry. The last term $< U_L|U_S|^2 >$ is related to the correlation between the long wave forced by the wave group and short wave velocity variance.

Firstly, the central, odd flow moment due to the wave asymmetry $< U_S|U_S|^2 >$ is calculated with the filtered high wave velocity U_s. The comparisons among measurements, result calculated by model of Roevink and Stive [21] and SWASH predictions are demonstrated in Figure 5-6. SWASH gave an overll good approximation especially before wave breaking(x<30 m). The results under influence of breaking show comparable differences which is probably due to the lack of breaking-induced turbulence in the SWASH.

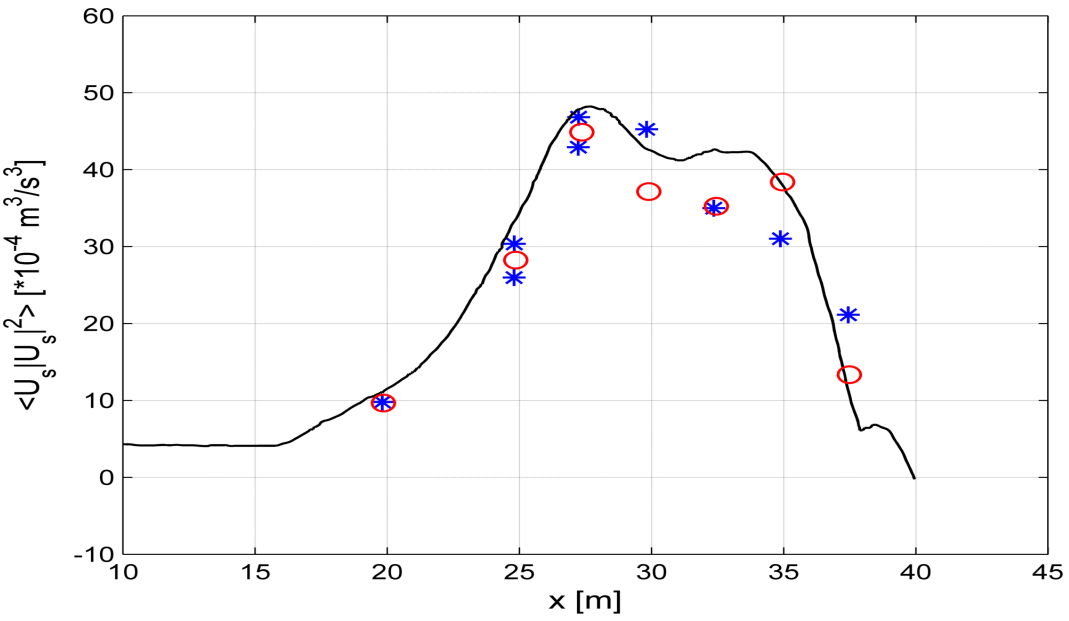

Figure 5-6: Central odd moment of wave-induced asymmetric flow $< U_S|U_S|^2 >$. Measurements(blue stars), Roelvink and Stive(black line) and SWASH predictions(red circles).

Subsequently, the central odd moment of time-varying velocity $< U_t|U_t|^2 >$ is presented in Figure 5-7. Here, $< U_t|U_t|^2 >=< U_S|U_S|^2 > +3 < U_L|U_S|^2 >$. As can be seen in the figure, the deviations between the SWASH results and observations are relatively large under influence of wave breaking. These deviation maybe associated to the differences resulted in Figure 5-5 and Figure 5-6.

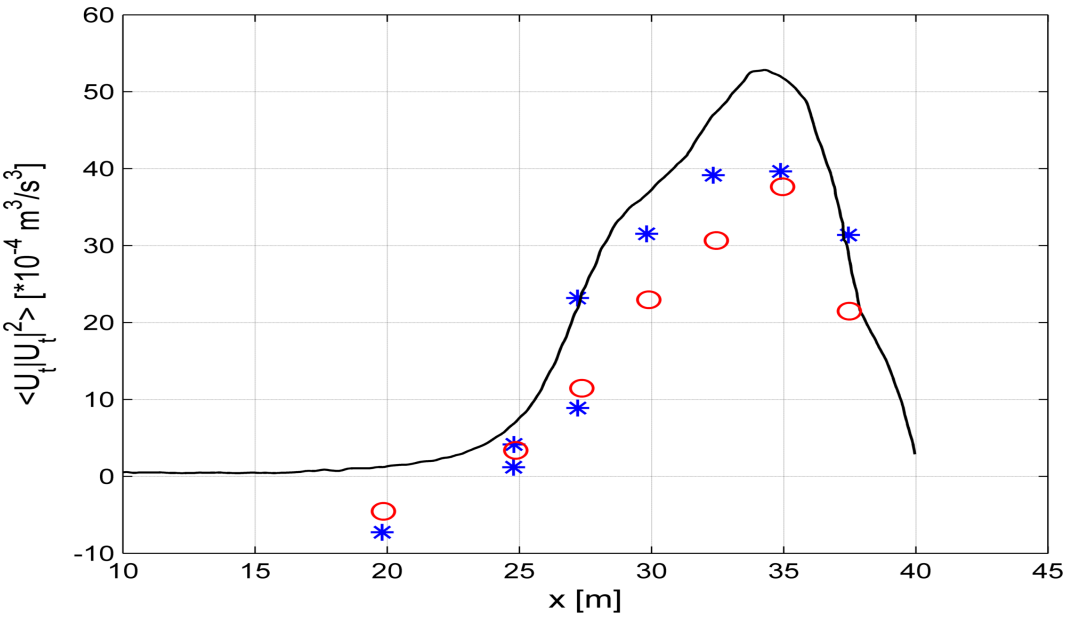

Figure 5-7: Central odd moment of time-varying component of total flow $< \tilde{U}|\tilde{U}|^2 >$. Measurements(blue stars), Roelvink and Stive(black line) and SWASH predictions(red circles).

To achieve the research objective, Figure 5-8 is presented to compare the contributed components to cross-shore odd velocity moment visually. In this manner, the significant contributions to the cross-shore sediment transport are hence known through the comparison. The relevant constituents of total odd flow moments are firstly discussed separately and the total flow is obtained by Eq. (5-2).

The orange crosses represent the computed results of the odd flow moments due to the wave asymmetry $< U_S|U_S|^2 >$ compared to the measurements indicated by blue diamonds and the model calculation of Roelvink and Stive [21] illustrated by orange line. As mentioned in Figure 5-6 that the SWASH predictions were in relatively good agreement to both measurements and model of Roelvink and Stive [21]. These non-linear central odd flow moments are all positive and the contribution of wave asymmetric flow to cross-shore transport is hence onshore-directed.

Moreover, the SWASH computed contribution of undertow $3 < \bar{U}|U_S|^2 >$ is demonstrated with black pluses while the black line represent the calculation of the model of Roelvink and Stive. It is evident that the SWASH predictions agree well to the result computed by Roelvink and Stive [21]. Since the undertow is the compensation for the mass flux between wave crest and trough which propagates perpendicular to the beach, the return flow is of course forcing the transport offshore. It can be seen in the Figure 5-8 that the magnitude of contribution of undertow is much larger than the other components. Therefore, the return flow under wave trough plays a relatively dominant role in cross-shore transport.

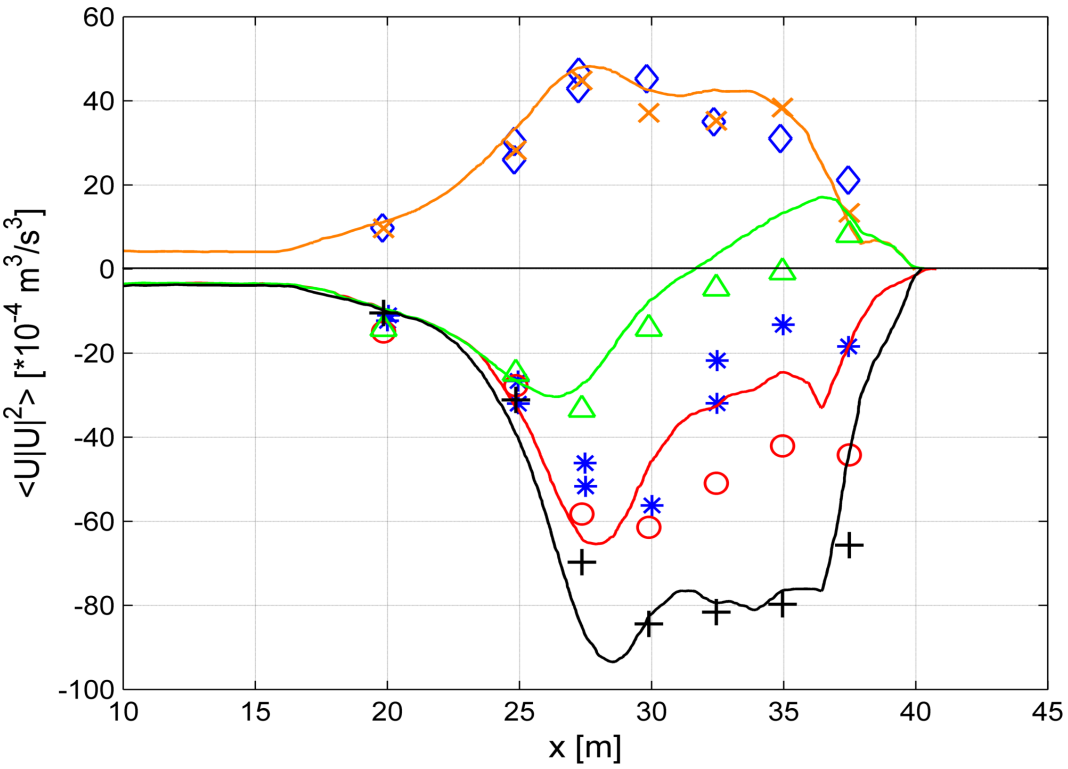

Figure 5-8: Total odd flow moments $< U|U|^2 >$ and contributed components. Total flow: measurements(blue stars), Roelvink and Stive(red line) and SWASH predictions(red circles); Asymmetric oscillatory flow: measurements(blue diamonds), Roelvink and Stive(orange line) and SWASH predictions(orange crosses); Wave grouping-induced long wave flow: Roelvink and Stive(green line) and SWASH predictions(green triangles); Undertow: Roelvink and Stive(black line) and SWASH predictions(black pluses).

In addition, the green triangles indicate the odd flow moment $3 < U_L|U_S|^2 >$, which is related to the correlation between the wave grouping-induced long wave and short wave velocity variance. However, the contribution of long wave flow is relatively underestimated comparing to the prediction of Roelvink and Stive(green line). As can be discovered in Figure 5-5, the variances of wave grouping-induced long wave flows were in good agreement with the measurements but smaller than the results of Roelvink and Stive after wave breaking. This underestimation is probably due to the smaller long wave flows. Another explanation could be the loss of information of correlation between long and short waves after Fourier and inverse Fourier transform, since the error induced by the filter is not easily avoided. Before the wave breaking, the bound long wave is still forced in the wave group. Figure 5-8 indicates that, the odd flow moments due to low frequency waves are negative in the deeper water(x< 32 m approximately) but positive in the shallow water. It could be explained by that, in the deep water the maximum shoreward orbital velocity is associated with a offshore-directed motion of the trough of bound long wave. After wave breaking, the bound long wave is released and then the sediment is transported in onshore direction by the free long waves.

Finally, the total flow can be obtained by adding the contributions mentioned above. It can be found that SWASH under-predicted the total odd flow moments after the breaking. This underestimation may correspond to the errors of three components. In general, the most likely reasons are the absence of turbulent production due to the roller and the inaccuracy of decomposition.

Nevertheless, SWASH gave an overall good predictions of the total odd flow moment as well as the components of contribution. It is obvious that the seaward undertow is the dominant component and the shoreward asymmetric flow is of importance as well. The contribution of long wave flow is relatively small but it cannot be ignored. To sum up, the total flow results in a offshore-directed transport, see Figure 5-8.

Chapter 6

Conclusions and Recommendations

This Chapter provides the main findings of the project, which are concluded in Section 6-1. Based on the conclusions, some recommendations for the future research are raised in 6-2.

6-1 Conclusions

The cross-shore sediment transport is one of the most critical determinants of the coastal profile evolution. The mechanism of the cross-shore sediment transport is incredibly complex to be simulated and hence in this study, we focus on the odd velocity moment proportional to the sediment movement. The contribution of the odd velocity moment is divided into three components, namely the undertow, the wave asymmetric flow and the wave grouping-induced long wave flow. To gain insight into these flow components in the coastal water, the non-hydrostatic SWASH is employed since it is capable of accurately simulating a number of wave phenomena in shallow water. In this study, an attempt is made to improve the understanding of how the flow components contribute to the cross-shore velocity moments.

Firstly, the methodology developed in this study is evaluated by means of reproducing the wave flume experiment of Roelvink and Stive [21]. The sensitivity of wave decay and mean velocity are assessed by varied settings in SWASH. The results show that SWASH is capable of giving overall good predictions of wave decay and vertical velocity with appropriate settings. Special attentions should be given to the imposition of bound long waves, the type of boundary condition and the discretization of water depth in velocity points. The former is of utmost importance in predicting water level, wave decay and vertical velocity in a accurate and stable manner and is hence included in the boundary condition. Moreover, the boundary condition is expected to be given by a spectrum file, containing the data of wave spectrum imposed in the flume test. However, a relatively small frequency interval is not applicable in SWASH yet and this could be improved in the future. For the discretization of water depth in velocity points, the central difference scheme provided better prediction for simulating the wave decay while the first order upwind scheme was recommended in the case of prediction of undertow. However, the results of second order interpolation augmented with MUSCL flux limiter and

central differencing showed relatively large error in this study, the inaccuracy may correspond to the instability due to their adoptions in SWASH.

After the optimum settings for simulating the wave decay and vertical velocity are determined, a detailed analysis is carried out to investigate the near-shore processes, including surface elevation, wave decay and undertow. In this study, the undertow is represented by the mean velocity at 5 cm above the bottom due to the location of the measurement. In fact, all the SWASH predictions are in relatively good agreement to the measurements, but the deviations cannot be ignored especially after wave breaking. This is most likely due to the absence of breaking-induced turbulence in SWASH.

In addition, a signal decomposition technique is applied in the following to extract low and high frequency components, respectively. In this way, the central odd moments due to long waves and asymmetric oscillatory flows can be obtained. The predictions of long wave flow variances and the central odd moments of asymmetric flows agree well to the observations. However, the central odd moment of grouping-induced long wave flow is underestimated. Excepting the reason of lacking roller in SWASH, another possibility would be the loss of signal due to decomposition.

Finally, the total flow can be obtained by adding the contributions of undertow, wave grouping-induced long wave flow and asymmetric oscillatory flow. The total flow is underestimated probably corresponding to the inaccuracy of predicting the flow components. However, SWASH still provides relatively good predictions of the total odd flow moments as well as its components of contribution. In general, the offshore-directed undertow is the dominant component, the shoreward asymmetric flow is of secondary importance and the contribution of long wave flow is relatively small. Therefore, the total flow results in a seaward sediment transport.

In summary, this study shows that SWASH is capable of simulating the wave decay and vertical flow structure correctly. The combination with a decomposition technique provides a routine to obtain the long and short wave flow components and hence the contributions of flow components to the cross-shore velocity moments. However, further development is required to improve the accuracy. In the next section, some recommendations are presented for the further study.

6-2 Recommendations

Based on the comparisons and analysis, it can be concluded that the combination of SWASH and decomposition is able to reproduce the cross-shore flows reasonably. In order to improve the accuracy of the results, the recommendations are listed in the following for future research.

1. Since the experiment applied the mean velocity at 5 cm above the bottom to represent the undertow, in this study the return flow is hence investigated in the same way. However, the undertow is defined as the mean velocity under the wave trough. It is recommended to model the flow structure along the water column. Therefore, an additional experiment of measuring the mean velocity in the whole water column is desired in the future research.

2. Even though the wave spectrum can be given in a file but a relatively small frequency interval is not applicable in SWASH yet. This option is recommended to be developed with higher resolution in frequency. In this case, the cycle period would not be too short resulting in unstable simulation and the inaccuracy of imposing boundary condition could be avoided as well.

3. Based on the sensitivity analysis, the wave decay and vertical velocity are relatively sensitive to varied schemes of discretization of water depth in velocity points. This may be caused by the instability corresponding to the application of the second order interpolation augmented with MUSCL flux limiter or central differencing. Hence, a further study is recommended to develop this model setting.

4. Most of the deviations occurred after wave breaking in this study. The lack of production of turbulence due to roller may be the dominant issue. As a result, the contribution of surface roller should be implemented in the SWASH.

5. Another possible reason to explain the difference might be the inaccuracy of decomposition. In this study, a simple filter to zero out the undesired frequency components is adopted. The accuracy of filter is not investigated. In the following study, it is valuable to evaluate different filters in the decomposition process.

Appendix A

Digitization of data

The data of the input topography and the compared measurements were obtained by means of digitizing the data from the images given by Roelvink and Stive [21]. In the following, the principle of acquiring data from an image file is described.

After loading the image file, the axes dimensions should be calibrated by graphically identified the origin and a value on x- and y- axis, respectively. The data points are subsequently obtained by clicking on the image, giving values of x and y. In this way, a set of data can be extracted to represent the points and lines that illustrated on the image. The MATLAB script can be obtained through the link: http://www.mathworks.com/matlabcentral/fileexchange/7173-grabit

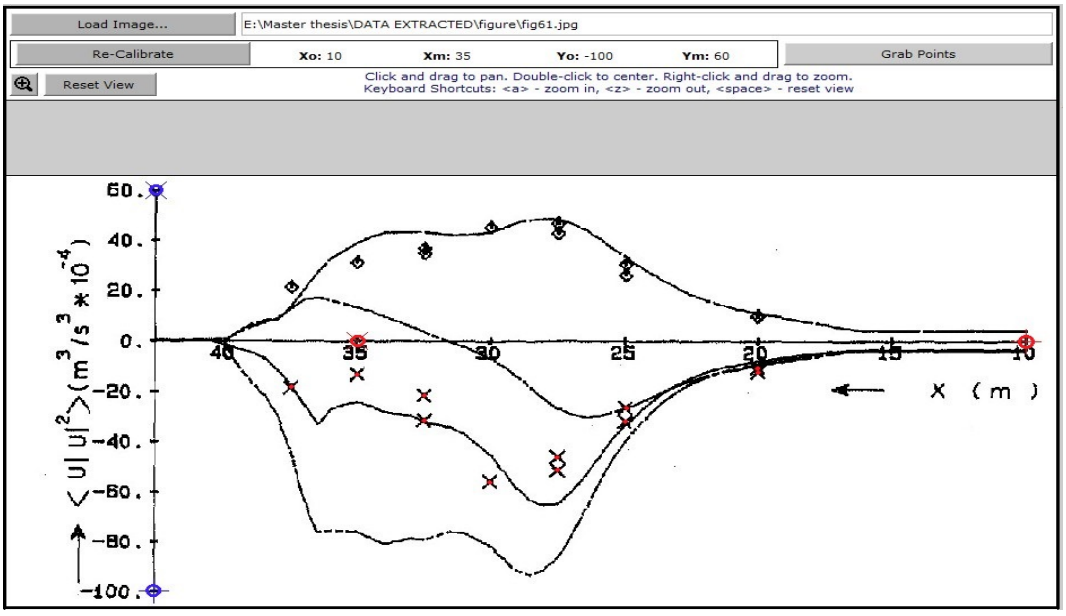

Figure A-1: Interface for grabbing data from image file

For example, Figure A-1 shows the interface for grabbing data from image file. Firstly, the x-axis was determined by two points x=10 and x=35 while y-axis was identified by y=-100 and y=60, see red and blue circles, respectively. Then the data indicating the cross was obtained by graphically clicking on the image, the red points in the middle of the crosses gave x and y values in a MATLAB file.

Appendix B

Command BREAK

SWASH considers the breaking waves as bores or hydraulic jump and the wave breaking-induced energy dissipation can be determined by ensuring the momentum conservation over the discontinuity near the surface. However, if a relatively coarse vertical resolution is adopted in the model, the phase velocity at the front face of breaking wave is approximated. In this way, the horizontal velocities near the wave crest as well as the dispersion of amplitude would be underestimated, resulting in underestimation of energy dissipation. Therefore, the command BREAK should be adopted to control wave breaking in a case of low vertical resolution.

The command BREAK is a trick to determine the onset and offset of the wave breaking by means of tracking the wave fronts. The wave breaking is initiated when the surface steepness exceeds a fraction of shallow water celerity, given by:

$$\frac{\partial \zeta}{\partial t} > \alpha \sqrt{gd} \tag{B-1}$$

The parameter α is the threshold value to initiate the onset of breaking. The process to terminate the wave breaking is the same as onset, but the threshold parameter is reduced to β:

$$\frac{\partial \zeta}{\partial t} > \beta \sqrt{gd}, \qquad with \beta < \alpha \tag{B-2}$$

A value of 0.6 is advised for the onset parameter α while the persistence parameter β is recommended to set to 0.3 according to calibration [22]. In this manner, the energy dissipation due to wave breaking might be correctly computed, based on momentum conservation, in a case of coarse vertical resolution.

Nonetheless, if relatively high vertical resolution(>10 layers) is adopted, this option should not be included in SWASH. Otherwise, the wave breaking-induced energy dissipation would be approximately incorrectly, see Figure B-1.

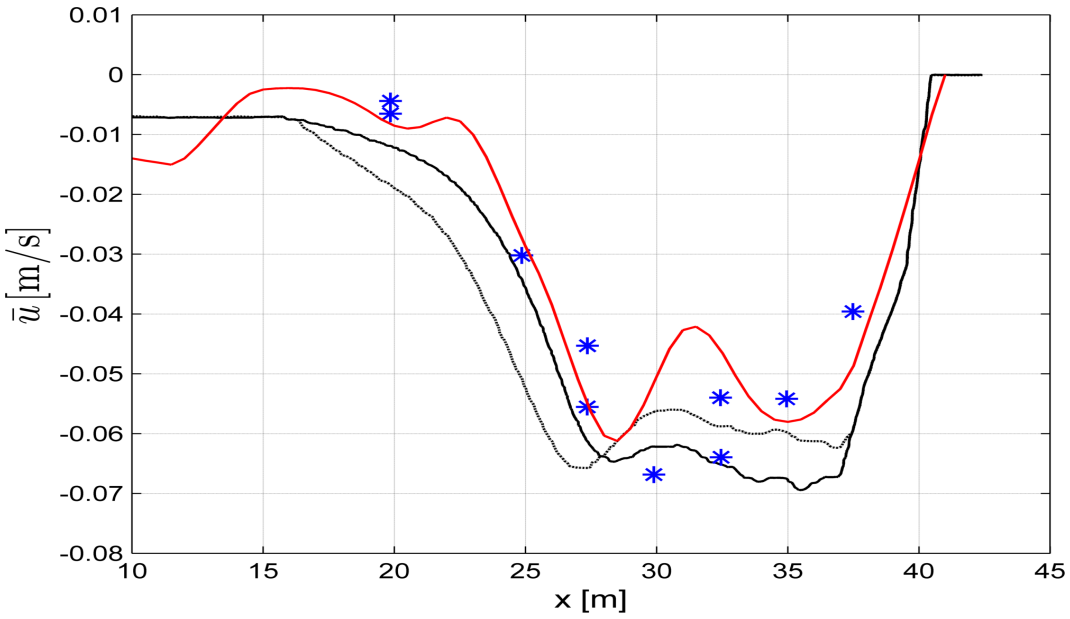

Figure B-1: Mean velocity at 5 cm above bottom with Command BREAK. Roelvink and Stive with lag(black solid line), Roelvink and Stive without lag(black dashed line), measurements(blue stars), SWASH prediction(red line).

As can be seen in the Figure B-1 that, a peak is shown near the breaking point. For the case with a sufficient number of layers, SWASH is able to calculate the phase velocity of the breaking front accurately. If the option BREAK is employed to control the wave breaking, the energy dissipation would be influenced, resulting in inaccurate approximation. Therefore, the command BREAK cannot be adopted in the case of relatively high resolution in the vertical.

Reference

[1] Bagnold, R. A. [1962]. Auto-suspension of transported sediment; turbidity currents, *Proceedings of the Royal Society of London. Series A, Mathematical and Physical Sciences* pp. 315–319.

[2] Bagnold, R. A. [1963]. Beach and nearshore processe-part 1, mechanics of marine sedimentation, *The Physics of Sediment Transport by Wind and Water* pp. 188–207.

[3] Bagnold, R. A. [1966]. An approach to the sediment transport problem from general physics, *US Geol. Surv. Prof. Pap., 422* **1**: 231–291.

[4] Bailard, J. A. [1981]. An energetics total load sediment transport model for a plane sloping beach, *Journal of Geophysical Research: Oceans (1978–2012)* **86**(C11): 10938–10954.

[5] Bailard, J. A. [1982]. Modeling on-offshore sediment transport in the surfzone, *Coastal Engineering Proceedings* **1**(18).

[6] Bailard, J. A. and Inman, D. L. [1981]. An energetics bedload model for a plane sloping beach: local transport, *Journal of Geophysical Research: Oceans (1978–2012)* **86**(C3): 2035–2043.

[7] Battjes, J. A. and Janssen, J. P. F. M. [1978]. Energy loss and set-up due to breaking of random waves, *Coastal Engineering Proceedings* **1**(16).

[8] Battjes, J. A. and Stive, M. J. F. [1985]. Calibration and verification of a dissipation model for random breaking waves, *Journal of Geophysical Research: Oceans (1978–2012)* **90**(C5): 9159–9167.

[9] Bowen, A. [1980]. Simple models of near-shore sedimentation; beach profiles and long-shore bars, *The Coastline of Canada, edited by S.B. McCann; Geological Survey of Canada, Pap. 80-10* pp. 1–11.

[10] Brinkkemper, J. A. [2013]. Modeling the cross-shore evolution of asymmetry and skewness of surface gravity waves propagating over a natural intertidal sandbar.

[11] Camenen, B., Larson, M. and Bayram, A. [2009]. Equivalent roughness height for plane bed under oscillatory flow, *Estuarine, Coastal and Shelf Science* **81**(3): 409–422.

[12] Cowell, P. J., Stive, M. J. F., Niedoroda, A. W., de Vriend, H. J., Swift, D. J. P., Kaminsky, G. M. and Capobianco, M. [2003]. The coastal-tract (part 1): a conceptual approach to aggregated modeling of low-order coastal change, *Journal of Coastal Research* pp. 812–827.

[13] Holthuijsen, L. H. [2007]. *Waves in oceanic and coastal waters*, Cambridge University Press.

[14] Kostense, J. [1984]. Measurements of surf beat and set-down beneath wave groups, *Coastal Engineering Proceedings* **1**(19).

[15] Launder, B. E. and Spalding, D. [1974]. The numerical computation of turbulent flows, *Computer methods in applied mechanics and engineering* **3**(2): 269–289.

[16] Launder, B. E. and Spalding, D. B. [1972]. Lectures in mathematical models of turbulence.

[17] Longuet-Higgins, M. S. [1953]. Mass transport in water waves, *Philosophical Transactions of the Royal Society of London. Series A, Mathematical and Physical Sciences* **245**(903): 535–581.

[18] Rijnsdorp, D. P. [2011]. Numerical modelling of infragravity waves in coastal regions.

[19] Rijnsdorp, D. P., Smit, P. B. and Zijlema, M. [2012]. Non-hydrostatic modelling of infragravity waves using swash, *Coastal Engineering Proceedings* **1**(33): currents–27.

[20] Rijnsdorp, D. P., Smit, P. B. and Zijlema, M. [2014]. Non-hydrostatic modelling of infragravity waves under laboratory conditions, *Coastal Engineering* **85**: 30–42.

[21] Roelvink, J. A. and Stive, M. J. F. [1989]. Bar-generating cross-shore flow mechanisms on a beach, *Journal of Geophysical Research: Oceans (1978–2012)* **94**(C4): 4785–4800.

[22] Smit, P., Zijlema, M. and Stelling, G. [2013]. Depth-induced wave breaking in a non-hydrostatic, near-shore wave model, *Coastal Engineering* **76**: 1–16.

[23] Stelling, G. and Duinmeijer, S. [2003]. A staggered conservative scheme for every froude number in rapidly varied shallow water flows, *International Journal for Numerical Methods in Fluids* **43**(12): 1329–1354.

[24] Stive, M. J. F. and De Vriend, H. J. [1987]. Quasi-3d nearshore current modelling: Wave-induced secondary current, American Society of Civil Engineers, pp. 356–370.

[25] Svendsen, I. A. [1984]. Mass flux and undertow in a surf zone, *Coastal Engineering* **8**(4): 347–365.

[26] team, T. S. [2014]. *SWASH user manual*, Delft University of Technology.

[27] Wright, L. D. [1995]. *Morphodynamics of inner continental shelves*, CRC Press.

[28] Zijlema, M. and Stelling, G. S. [2005]. Further experiences with computing non-hydrostatic free-surface flows involving water waves, *International journal for numerical methods in fluids* **48**(2): 169–197.

[29] Zijlema, M., Stelling, G. and Smit, P. [2011]. Swash: An operational public domain code for simulating wave fields and rapidly varied flows in coastal waters, *Coastal Engineering* **58**(10): 992–1012.